

Contents

1 Theory	3
1.1 X-ray Diffraction Principles	3
1.1.1 Scattering at Lattices	3
1.1.2 X-rays	5
1.2 Sesquioxides	5
1.2.1 Chromium Oxide	6
1.2.2 Gallium Oxide	8
1.3 Heteroepitaxy	9
1.3.1 Pseudomorphic Growth	9
1.3.2 Relaxed Growth	11
Dislocations	11
Slip Systems for Sesquioxide Heterostructures	13
2 Experimental Methods	15
2.1 Pulsed Laser Deposition	15
2.1.1 Setup	16
2.1.2 Plasma Dynamics	16
2.1.3 Segmented Target Approach	18
2.2 X-Ray Diffraction Measurement	18
2.2.1 2θ - ω -scans	19
2.2.2 ω -scans	20
2.2.3 φ -scans	20
2.2.4 Reciprocal Space Maps	21
2.2.5 Technical Aspects	23
2.3 Further Methods	24
2.3.1 Thermal Evaporation	24
2.3.2 Resistivity Measurement	25
2.3.3 Thickness Determination	26
2.3.4 Spectral Transmission	27
3 Experiment, Results and Discussion	29
3.1 Preliminary Investigations	29
3.1.1 Experiment	29
3.1.2 Results	30
Oxygen Partial Pressure Variation on <i>m</i> -plane Sapphire	30
Growth Temperature Variation on <i>m</i> -plane Sapphire	32
Influence of Growth Rate on Crystal Structure	33

	Deposition on <i>c</i> -, <i>r</i> -, <i>m</i> - and <i>a</i> -plane Sapphire	36
3.1.3	Conclusion	38
3.2	Doping of Cr ₂ O ₃ Thin Films	40
3.2.1	Experiment	40
3.2.2	Results	41
	Laser Position Variation for Different Targets	41
	Ohmic Contact Optimization	48
3.2.3	Conclusion	48
3.3	Strain Analysis	50
3.3.1	Experiment	50
	Sample Fabrication	50
	Measurements	51
3.3.2	Results	53
	Strain for <i>c</i> -plane Thin Films	55
	Appendices	57
	A Calculations	59
A.1	<i>m</i> -plane lattice constants	59
A.2	<i>a</i> -plane lattice constants	59
	B Figures	61

Chapter 1

Theory

Contents

1.1 X-ray Diffraction Principles	3
1.1.1 Scattering at Lattices	3
1.1.2 X-rays	5
1.2 Sesquioxides	5
1.2.1 Chromium Oxide	6
1.2.2 Gallium Oxide	8
1.3 Heteroepitaxy	9
1.3.1 Pseudomorphic Growth	9
1.3.2 Relaxed Growth	11

1.1 X-ray Diffraction Principles

1.1.1 Scattering at Lattices

To elucidate the working principles behind X-ray diffraction (XRD) as a measurement method (cf. 2.2), a brief description of reciprocal space and constructive interference will be provided. Those derivations are based on Ashcroft and Mermin (1976) [1].

A periodic point-like structure with translational symmetry (“BRAVAIS lattice”) can be described by three vectors \mathbf{a}_i that span a so-called “unit cell”. Every lattice point \mathbf{R} is a linear combination of those unit cell vectors. For such a lattice, there exists a so-called “reciprocal lattice”, which consists of all vectors \mathbf{K} satisfying the condition⁽¹⁾:

$$e^{i\langle \mathbf{K}, \mathbf{R} \rangle} = 1. \quad (1.1)$$

This is again a BRAVAIS lattice with unit cell vectors \mathbf{a}_j^* :

$$\mathbf{K}_{hkl} = h\mathbf{a}_1^* + k\mathbf{a}_2^* + l\mathbf{a}_3^*. \quad (1.2)$$

⁽¹⁾ The definition of \mathbf{K} by (1.1) is a consequence of demanding that the plane wave described by $f_{\mathbf{K}}(\mathbf{r}) = \exp(i\langle \mathbf{K}, \mathbf{r} \rangle)$ has the same symmetry as the BRAVAIS lattice [1].

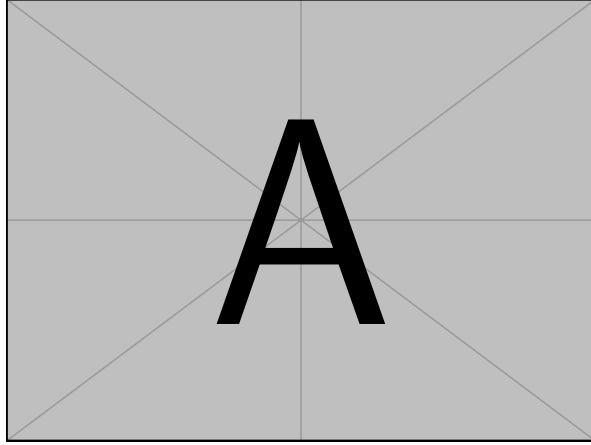


Figure 1.1: Here comes an ashcroft-like image for the scattering geometry to derive Equ. (1.6)

It follows that for any i, j :

$$\langle \mathbf{a}_i^*, \mathbf{a}_j \rangle = 2\pi\delta_{ij}, \quad (1.3)$$

with the KRONECKER delta δ_{ij} . A major application of reciprocal space vectors is their ability to describe lattice planes. Any lattice plane can be described by the shortest possible reciprocal space vector \mathbf{K}_{hkl} perpendicular to it. Consequently, the lattice plane is denoted by (hkl) . The distance between equivalent lattice planes can be calculated via

$$d_{hkl} = |\mathbf{K}_{hkl}|^{-1}. \quad (1.4)$$

Note that for non-cubic crystals, the lattice plane (hkl) is in general *not* perpendicular to the lattice direction $[hkl]$.

With those preliminaries, the conditions for constructive interference during diffraction of radiation at BRAVAIS lattices can be derived. Consider two scattering centers separated by \mathbf{d} . Now consider incoming radiation with wave vector \mathbf{k} :

$$\mathbf{k} = \frac{2\pi}{\lambda}\hat{\mathbf{n}}, \quad (1.5)$$

with wavelength λ and direction $\hat{\mathbf{n}}$. For the case of elastic scattering, the outgoing wave vector \mathbf{k}' has the same wavelength λ but different direction $\hat{\mathbf{n}'}$. The phase difference of two photons scattered at the 1st and 2nd scattering center, respectively, can be calculated from their path difference, which reads

$$\langle \mathbf{d}, \hat{\mathbf{n}} \rangle + \langle -\mathbf{d}, \hat{\mathbf{n}'} \rangle. \quad (1.6)$$

Constructive interference occurs, if the phase difference is an integral multiple of the wavelength, so it must follow that

$$\langle \mathbf{d}, (\hat{\mathbf{n}} - \hat{\mathbf{n}'}) \rangle = m\lambda \quad (1.7)$$

$$\Leftrightarrow \langle \mathbf{d}, (\hat{\mathbf{k}} - \hat{\mathbf{k}'}) \rangle = 2\pi m, \quad (1.8)$$

with $m \in \mathbb{N}$. Comparing with (1.1) reveals that $\hat{\mathbf{k}} - \hat{\mathbf{k}'}$ is a reciprocal space vector, because the separation \mathbf{d} of the two scattering centers is a lattice vector. So constructive

interference (observing a reflex) occurs if and only if the scattering geometry (determined by angle of incidence and refraction, as well as wavelength) matches the lattice symmetry in the sense that there is a corresponding lattice translation vector \mathbf{d} fulfilling Equ. (1.8). So from the “position” of reflexes, one can deduce the lattice symmetry.

Note that this description of X-ray scattering is equivalent to the BRAGG condition:

$$m\lambda = 2d_{hkl} \sin(\theta), \quad (1.9)$$

where the angle of incidence θ and λ are contained in $\hat{\mathbf{k}} - \hat{\mathbf{k}}'$. Furthermore, when a lattice point is not equivalent to a single atom, but represents several scattering centers, an additional geometrical structure factor has to be taken into account to determine whether a certain geometry allows reflexes. This is important, e.g., for structures with trigonal symmetry. They are described with a conventional hexagonal unit cell, although not every plane (hkl) exhibits constructive interference.

1.1.2 X-rays

Atomic distances in solids are of the order of several Å, so the radiation for probing those structures must have a similar wavelength, which turns out to be X-rays [2]. The following description of X-rays is based on Spieß (2009) [3].

The basis of any X-ray tube are high-energy electrons which are produced by thermionic emission in a cathode, which is usually made out of tungsten⁽²⁾. An electric field of several kV accelerates the electrons to the anode, where they are stopped such that around 99 % of their kinetic energy dissipates. The momentum change of electrons, which are charged particles, leads to emission of *bremsstrahlung*. Furthermore, the electrons ionize atoms of the anode material which leads to unoccupied electron states. If those states are filled by electrons with higher quantum number n , the difference in energy of those levels is emitted as radiation with a discrete spectrum, called characteristic X-ray. Important for this work is a part of the characteristic spectrum, called K-radiation, which originates in occupation of empty $1s$ -orbitals. The occupying electron must come from an orbital with angular momentum quantum number $l = 1$, i.e. a p -orbital, because Δl cannot be zero. The radiation is termed $K\alpha$ - or $K\beta$ -radiation, if the previous orbital was $2p$ or $3p$, respectively. Furthermore, one distinguishes $K\alpha_1$ - and $K\alpha_2$ -radiation, depending on the magnetic quantum number of the previous orbital, which can be $\frac{3}{2}$ or $\frac{1}{2}$, respectively. $K\alpha$ -radiation is desired for probing crystal structures.

1.2 Sesquioxides

Transparent Conductive Oxides (TCOs) are materials that combine the properties of having low absorption coefficient in the visible spectrum and being conductive at the same time [4]. The interest in these materials is motivated by possible usage in portable and flexible electronics, displays, solar cells and more [5]. Due to the restriction on only a few materials in the industry (e.g. SnO_2 and In_2O_3), investigations of new materials are

⁽²⁾ Tungsten is the element with the second highest melting point of around 3400 °C. This ensures a low contamination of the anode with cathode material.

	<i>a</i>	<i>c</i>	Ref.
$\alpha\text{-Al}_2\text{O}_3$	4.76 Å	13.00 Å	Pishchik et al. (2009) [20]
$\alpha\text{-Cr}_2\text{O}_3$	4.96 Å	13.59 Å	Mi et al. (2018) [13]
$\alpha\text{-Ga}_2\text{O}_3$	4.98 Å	13.43 Å	Marezio and Remeika (1967) [21]

Table 1.1: Lattice constants of selected corundum structured compounds.

required [5]. This includes fabrication of *p*-type TCOs as well as compounds with even larger band gaps than 3 eV, called Ultrawide-bandgap (UWBG) materials. A candidate for the latter is Ga_2O_3 with its several polymorphs [6], where the corundum structured $\alpha\text{-Ga}_2\text{O}_3$ gained interest, even though its deposition has to account for parasitic growth of the thermodynamically more stable β -phase [7].

At this point, Cr_2O_3 comes in handy being a possible *p*-type TCO as well as being isomorphic to group-III sesquioxide $\alpha\text{-Ga}_2\text{O}_3$ with quite similar lattice parameters (cf. Tab. 1.1). This enables the use of Cr_2O_3 as a buffer layer between $\alpha\text{-Ga}_2\text{O}_3$ and isomorphic $\alpha\text{-Al}_2\text{O}_3$ (sapphire) substrates to improve the deposition process [8]. Furthermore, Cr_2O_3 exhibits increased conductivity upon doping [9] and could thus serve as *p*-type component in a *p-n*-heterojunction with $\alpha\text{-Ga}_2\text{O}_3$. In the following, an overview of the two mentioned sesquioxides will be provided with focus on the physical properties being relevant to this work.

1.2.1 Chromium Oxide

“Chromia” or “Eskolaite” is a sesquioxide composed of the transition metal chromium and oxygen with formula unit Cr_2O_3 . Among other chromium oxides (e.g. metallic CrO_2 , toxic CrO_3 etc.), it is the thermodynamically most stable phase [10–12], making it the abundant chromium oxide on earth [13]. Cr_2O_3 occurs mainly in the α -phase (described below), but a cubic spinel γ -phase with random missing Cr point defects has also been reported [10]. Henceforth, “ Cr_2O_3 ” will refer to the α -phase.

As coating material, Cr_2O_3 is commonly used due to its high hardness and resistance against corrosion [11, 14], also explaining its use-case as component of stainless steel to form passive films [12]. Cr_2O_3 thin films absorb electromagnetic waves with wavelengths smaller than 400 nm, making it opaque in the UV-spectrum [15, 16]. It is transparent in the visible spectrum with, e.g., a reported transmittance of 40 % at 700 nm for 0.5 µm thick films by Cheng et al. (1996) [15].

Cr_2O_3 crystallizes in the corundum structure, which has trigonal symmetry (space group $R\bar{3}c$) and belongs to the hexagonal crystal family. One unit cell contains six formula units, i.e. 12 chromium cations and 18 oxygen anions [12]. The oxygen atoms arrange in a hexagonal close-packed manner, where two thirds of the formed octahedrons are filled with Cr atoms [17]. The unit cell is spanned by a principal axis, called *c*-axis⁽³⁾, and a hexagonal basal plane with lattice constant *a*. The numerical values for those lattice parameters differ depending on the publication [4, 8, 13, 18, 19], and we will use the values in Tab. 1.1.

⁽³⁾ The spins of the Cr atoms along this direction are alternating $3 \uparrow$ and $3 \downarrow$ [4], making the crystal antiferromagnetic [12, 17].

Several techniques were applied for depositing chromia thin films, including: Chemical Vapor Deposition (CVD) [22–24] on silicon and glass, Molecular Beam Epitaxy (MBE) on sapphire [4, 25], thermal evaporation on platinum [10], electron-beam evaporation on glass [11], spray pyrolysis on glass [26], radio-frequency (RF) sputtering on sapphire [8, 27, 28], reactive direct current (DC) sputtering on glass [16], reactive Pulsed Laser Deposition (PLD) on silicon [29] and sapphire [30], and non-reactive PLD on sapphire [4, 14, 31].

Electronic Structure Experimental and theoretical studies reveal that chromia exhibits a band gap of 3.2 to 3.4 eV [10, 12, 13, 19] making it a wide band gap material. This predicts insulating behavior [19], classified as both Mott-Hubbard type and charge-transfer type, which are models to describe the electronic behavior of compounds containing transition metals with partly filled $3d^n$ orbitals⁽⁴⁾ [12, 13, 17]: Density Functional Theory (DFT) calculations show that the Cr-3d states are almost solely responsible for electronic states in the conduction band and that they are also present in the valence band [12, 13]. Thus, $3d \rightarrow 3d$ band transitions are possible, favoring the Mott-Hubbard model of this compound [12]. Furthermore, the O-2p states are mainly present in the valence band, at similar energies as the Cr-3d states, which leads to hybridization and thus favoring the charge-transfer model [12].

However, several studies agree on Cr_2O_3 being a semiconductor with *p*-type conductivity⁽⁵⁾ at room temperature and atmospheric conditions [12–15, 27, 29, 32]. Calculating the impact of different crystal point defects on the band structure may give insight into these observations. Indeed, when considering a missing chromium atom (“vacancy” V_{Cr}) the band structure changes in two ways: The band gap itself is reduced [13], but not in a way that it would make excitations of valence electrons into the conduction band much more probable than for defectless chromia. But additionally, there is a new band introduced slightly above the Fermi level (cf. Fig. 1.2), which acts as an unoccupied acceptor level [13]. This defect state is mainly composed of O-2p orbitals of the oxygen anions surrounding the vacancy [12]. From a more intuitive point of view, a missing neutral chromium atom effectively removes the Cr^{3+} cation as well as three electrons bound to the adjacent O^{2-} anions, thus creating three holes [12] explaining the *p*-type conductivity.

Note that there are also other possible defects with different effects: a chromium Frenkel point defect describes a Cr atom leaving its position and occupying a formerly unoccupied cavity in one of the oxygen-octahedrons. This Frenkel defect actually creates a new band right below the Fermi level, acting as an occupied donor level [12]. A similar defect state is introduced by oxygen vacancies [13]. But note that the Fermi level is located only slightly above the Valence Band Maximum (VBM) and thus the new occupied donor level is not significantly closer to the Conduction Band Minimum (CBM), which means that electrons still have to overcome the band gap energy to get into conducting states. This favors the formation of holes via Cr vacancies (O-2p accep-

⁽⁴⁾ $n = 5$ for Cr

⁽⁵⁾ Cheng et al. (2001) [23] actually find Cr_2O_3 to be insulating. It is noted that they examined Cr_2O_3 as an 2 nm thick oxide surface on CrO_2 films deposited by CVD. Farrell et al. (2015) [25] also find that their high quality epitaxial films of Cr_2O_3 grown by MBE exhibit no *p*-type conductivity. Similar results were found by Kehoe et al. (2016) [4] for MBE and PLD deposited films.

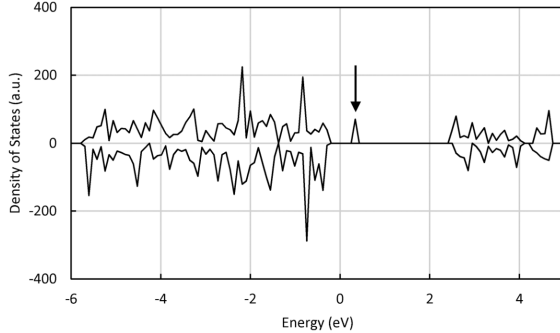


Figure 1.2: Calculated density of states (DOS) of chromia, taking a V_{Cr} into account. The arrow marks the new acceptor level. Image taken from [12].

tor states) rather than electrons via Cr Frenkel defects and O vacancies (Cr-3d donor states).

Doping Several attempts have been made to alter the conductivity of chromia thin films deliberately, including incorporation of magnesium, nickel, or lithium to achieve better *p*-type conductivity [25]. On the other hand, incorporating titanium seems to yield electrons as majority carriers [33] due to the higher valent state of Ti when substituting Cr sites (Ti_{Cr}) [32].

Due to interest in the electrical properties of *p*-type TCOs, the influence on Mg-doped Cr_2O_3 thin films has been investigated by several studies [4, 9, 19, 25, 26, 31, 33]. Substituting Cr atoms with less valent hole providers – compared to structural defects of pure Cr_2O_3 – does not only allow for a more controlled defect incorporation, but is also energetically more favorable due to a lower formation energy of Mg_{Cr} compared to V_{Cr} [4]. Uekawa and Kaneko (1996) [9] report an increase in conductivity of five orders of magnitude for $\text{Cr}_2\text{O}_3:\text{Mg}$ thin films. This result can be further improved by postannealing [25] and deposition at higher oxygen partial pressures [25, 33]. These effects are attributed to homogenization of magnesium inside the thin films and increased MgO incorporation during deposition, respectively. An observed side-effect of Mg-doping is a color change to a brownish tint [9, 19]. Uekawa and Kaneko (1996) [9] discuss that this may be the result of a mixed valence state of chromium (Cr^{4+} or Cr^{6+}), formed upon doping, as observed by X-ray Photoelectron Spectroscopy (XPS). This may establish an unoccupied state, favoring charge-transfer transitions from $\text{O}-2p$ orbitals to this low-energetic state, resulting in a different visual appearance of the thin films. However, it has been shown that the overall transparency can be increased by codoping of Mg with nitrogen which also reduces the decolorization substantially [19, 26].

1.2.2 Gallium Oxide

Ga_2O_3 is a group-III sesquioxide with four different polymorphs, of which $\beta\text{-}\text{Ga}_2\text{O}_3$ is the thermodynamically most stable one at ambient conditions [6, 7, 34]. The corundum-structured $\alpha\text{-}\text{Ga}_2\text{O}_3$ phase, which is of more relevance for this work, is isomorphic to Cr_2O_3 (cf. 1.2.1), with lattice parameters as listed in Tab. 1.1. $\alpha\text{-}\text{Ga}_2\text{O}_3$ is metastable [35], i.e. not favored in the first place, but remains irreversibly after formation, e.g.,

after phase transition from β - to α -phase at high temperatures [36]. The thermodynamic equilibrium – which determines the favored phase – can also be changed by strain due to lattice mismatch occurring during heteroepitaxy⁽⁶⁾ [34]. This approach is of particular interest due to the possibility of deposition on cheap⁽⁷⁾ and readily available sapphire substrates which are isomorphic to $\alpha\text{-Ga}_2\text{O}_3$ [28, 35, 36]. Note that deposition of $\beta\text{-Ga}_2\text{O}_3$ on sapphire is also possible, but only with restriction to formation of more than one crystal domain [37]. On the other hand, highly crystalline [36] $\alpha\text{-Ga}_2\text{O}_3$ thin films should be able to be grown without rotational domains [37].

Deposition of $\alpha\text{-Ga}_2\text{O}_3$ on sapphire has been done by several deposition techniques, including [37]: Halide Vapor Phase Epitaxy (HVPE), mist CVD [38], MBE [34], Atomic Layer Deposition and metalorganic CVD. Phase-pure deposition via PLD has also been achieved [7, 34]. Despite being isomorphic to each other, $\alpha\text{-Ga}_2\text{O}_3$ and sapphire still exhibit a lattice mismatch of around 4.8 % along the a -axis [35]. This induces semi-coherent growth with a fairly high dislocation density, which has been reported to be around $7 \times 10^{10} \text{ cm}^{-2}$ [38]. In particular, this becomes a problem regarding carrier mobility which is tremendously hindered by dislocation scattering [35].

To overcome the problems of lattice mismatch between sapphire substrates and $\alpha\text{-Ga}_2\text{O}_3$ thin films, quasi-continuous gradients from Al_2O_3 to $\alpha\text{-Ga}_2\text{O}_3$ have been applied, utilizing the capability of alloying the respective compounds [39]. Furthermore, buffer layers of isomorphic Cr_2O_3 have been used to decrease the high dislocation density for deposition on c -oriented [8, 27] as well as r -oriented sapphire [28]. Deposition on other than c -oriented substrates also seems to decrease parasitic phases, because the suppression of crystal facets perpendicular to the principal c -axis may increase phase purity [40]. It has to be noted that despite the difficulties occurring upon lattice mismatch, coherent growth seems to be feasible without buffer layers for different deposition techniques, at least for some monolayers [34].

With 5.0 to 5.3 eV [37], $\alpha\text{-Ga}_2\text{O}_3$ has the highest band gap of the four polymorphs [36]. Increasing or decreasing the band gap is possible by alloying with Al_2O_3 [40] or In_2O_3 [41], respectively. The crystal structure also allows for alloying with other corundum structured compounds [37], in particular other transition metal oxides such as Cr_2O_3 [27, 28]. The conduction band is mainly composed of Ga-4s states with an effective electron mass of $0.3 m_e$. The valence band is very flat and mainly composed of O-2p orbitals, yielding a high effective electron mass and thus strong localization [36]. Next to band gap engineering, n -type doping via Sn or Si incorporation has been accomplished [37].

1.3 Heteroepitaxy

1.3.1 Pseudomorphic Growth

Comment: Ist der folgende Absatz zu lang, dafür dass ich (wahrscheinlich) nur bei c-Orientierung pseudomorphic growth beobachte? Aber ich wollte gerne ausrechnen, was denn

⁽⁶⁾ However, the possibility of formation of parasitic β -phase still has to be taken into account [7].

⁽⁷⁾ Compared to bulk $\beta\text{-Ga}_2\text{O}_3$ substrates [35, 37].

Table 1.2: The six independent entries of the elasticity tensor for rhombohedral Cr₂O₃ [44] and α -Ga₂O₃ [43]. All values are in units of 100 GPa.

Material	C_{11}	C_{12}	C_{13}	C_{33}	C_{44}	C_{14}
α -Cr ₂ O ₃	3.74	1.48	1.75	3.62	1.59	-0.19
α -Ga ₂ O ₃	3.82	1.74	1.26	3.46	0.78	-0.17

der out of plane strain wäre, falls es so sein sollte, damit ich später argumentieren kann, ob ich relaxed oder pseudomorphic beobachte; oder was dazwischen. Dementsprechend hab ich mich dann gezwungen gefühlt, das ganze noch mal aufzurollen. Vielleicht wäre eine Lösung, (1.11), (1.12) und (1.13) in eine Art appendix zu tun?

When a body is deformed (“strained”) from its original state of equilibrium (“bulk”), forces will arise that tend to return the body to this equilibrium. Molecular forces are the driving element behind these so-called stresses [42]. In continuum mechanics, stress σ_{ij} and strain ϵ_{kl} are symmetric rank-2 tensors that are linearly connected by the elasticity tensor with components C_{ijkl} :

$$\sigma_{ij} = C_{ijkl}\epsilon_{kl}, \quad (1.10)$$

which represents a set of linear equations⁽⁸⁾.

If the in-plane (i.p.) lattice constants of two isomorphic compounds match at the interface of a heterostructure, one refers to “pseudomorphic” growth. This case confines some equations of (1.10):

1. The thin film i.p. lattice constants have to match the substrate i.p. lattice constants. This defines the magnitude of i.p. strain of the thin film material.
2. On the other hand, due to vertical growth, the out-of-plane (o.o.p.) stress of the thin film is demanded to be zero.

The resulting o.o.p. strain as well as non-diagonal strain components can be derived by solving the system of equations (1.10) with these two boundary conditions. In Ref. [43], formulas are derived for the unknown strains in the special case of pseudomorphic heterostructures with threefold rhombohedral symmetry. For numerical predictions of those strains, the elasticity tensor C_{ijkl} of the thin film compound has to be known. Depending on the symmetry of the crystal structure, its components collapse into a lower number of independent entries⁽⁹⁾: for rhombohedral crystals, six independent components are left [1]. An example of the entries of the elasticity tensor for two sesquioxides is given in Tab. 1.2.

Because of its direct influence on the o.o.p. lattice plane distance and thus on the XRD patterns (cf. 1.1.2), the strain component perpendicular to the sample surface, ϵ_{zz} ,

⁽⁸⁾ Summation over same indices.

⁽⁹⁾ Due to symmetry reasons [1], the nine indices ij of the strain tensor can be unambiguously expressed by one index with six possible values: 11 → 1, 22 → 2, 33 → 3, 23 → 4, 13 → 5, 12 → 6 [43]. This allows for a 6×6 -matrix representation of the elasticity tensor $C_{ijkl} \rightarrow C_{\mu\nu}$.

is of particular interest. In the following, the relevant formulas are stated as derived in Ref. [43]. They depend on the respective i.p. strains ϵ_{xx} and ϵ_{yy} caused by the lattice mismatch between film and substrate. Note that here, $\mathbf{r} = (x, y, z)$ describes coordinates in the laboratory system – in contrary to Ref. [43], where \mathbf{r} and \mathbf{r}' are used to describe cartesian coordinates in the crystal and laboratory system, respectively.

One derives for (11.0)-plane (*a*-orientation):

$$\epsilon_{zz,a} = -\frac{C_{13}\epsilon_{xx,a} + C_{12}\epsilon_{yy,a}}{C_{11}}, \quad (1.11)$$

for (10.0)-plane (*m*-orientation):

$$\epsilon_{zz,m} = -\frac{C_{13}C_{44}\epsilon_{xx,m} + (C_{12}C_{44} + C_{14}^2)\epsilon_{yy,m}}{C_{11}C_{44} - C_{14}^2}, \quad (1.12)$$

and for (00.1)-plane (*c*-orientation):

$$\epsilon_{zz,c} = -\frac{2C_{13}}{C_{33}}\epsilon_{yy,c}, \quad (1.13)$$

with $\epsilon_{xx,a} = c_S/c_F - 1$ and $\epsilon_{yy,a} = a_S/a_F - 1$, depending on the lattice parameters of substrate (a_S , c_S) and film (a_F , c_F). Note that

$$\begin{aligned} \epsilon_{xx,a} &= \epsilon_{xx,m}, \\ \epsilon_{yy,a} &= \epsilon_{yy,m}, \\ \epsilon_{yy,c} &= \epsilon_{yy,a}. \end{aligned}$$

For (01.2)-plane (*r*-orientation), the formula gets longer and can be calculated as demonstrated in Grundmann (2020) [45]. The distance of lattice planes d orthogonal to the sample surface are then strained, such that:

$$d_{\text{strained}} = d(1 + \epsilon_{zz}). \quad (1.14)$$

Assuming pseudomorphic growth of Cr_2O_3 on Al_2O_3 , one can compare the strained lattice plane distances to the unstrained bulk values, by utilizing (1.14). The numerical values, calculated from the lattice constants (Tab. 1.1) and the elasticity tensor (Tab. 1.2), are listed in Tab. 1.3a.

1.3.2 Relaxed Growth

Dislocations

When the lattice mismatch is not resolved by adaption to the substrate (cf. 1.3.1), the periodicity of the film must be disrupted via so-called dislocations to facilitate relaxed growth of the film [46]. The highest disturbance from equilibrium spacing happens close to the so-called dislocation line which draws through the material – far away from this line, the crystallinity is restored. In which fashion the distortion happens, can be characterized by the BURGER's vector \mathbf{b} . The relation of the BURGER's vector to the dislocation line determines the type of the dislocation: if they are orthogonal, one refers to an *edge* dislocation; if they are parallel, one refers to a *screw* dislocation. For

Table 1.3: (a) Comparison of d and d_{str} , which are the o.o.p. lattice plane distances for bulk Cr_2O_3 and pseudomorphic Cr_2O_3 on Al_2O_3 , respectively. The corresponding o.o.p.-strain ϵ_{zz} is also given, as well as the corresponding angles of reflection for $2\theta\text{-}\omega$ -scans. (b) The resulting tilt of the thin film depending on substrate orientation for relaxed growth. The results follow from considerations on the possible slip systems and BURGER's vectors.

Orientation (X-ray reflection)	(a) Pseudomorphic					(b) Relaxed	
	d (nm)	d_{str} (nm)	ϵ_{zz} (%)	2θ ($^{\circ}$)	$2\theta_{\text{str}}$ ($^{\circ}$)	$\theta_{T,x}$	$\theta_{T,y}$
c (00.6)	13.59	14.12	3.90	39.75	38.20	—	—
a (11.0)	2.48	2.57	3.63	36.18	34.87	no	no
m (30.0)	4.30	4.45	3.67	65.06	62.49	yes	no
r (02.4)	3.63	3.72	2.41	50.19	48.93	yes	no

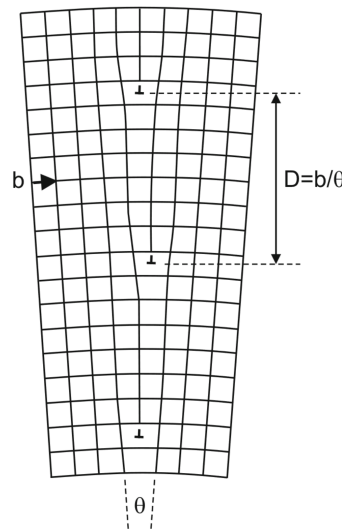


Figure 1.3: Edge dislocation with BURGER's vector perpendicular to sample surface. The normal to the surface draws horizontally in this picture. Taken from Grundmann (2016) [47] *tbd*

a so-called “perfect” dislocation⁽¹⁰⁾, the BURGER’s vector is a lattice translation vector. Note that in general, dislocations exhibit both edge- and screw-character [48].

Dislocations are not static, but can move (“glide”) inside the crystal. The movement happens typically inside a plane which has highest density of atoms (“glide plane”) and along the BURGER’s vector which is responsible for the dislocation [48]. The arrangement of glide plane and direction of movement is called “slip system”, e.g. for hexagonal structures, one finds $\{00.1\}/\langle 11.0 \rangle$ to be one prevailing slip system [48].

For heterostructures with certain slip systems, the relaxation results in an additional tilt of the deposited film. This happens because a BURGER’s vector \mathbf{b} has more than one component: the edge component b_{\parallel} causes strain relaxation along b_{\parallel} ; but if \mathbf{b} also exhibits a component b_{\perp} orthogonal to the sample surface and the dislocation line, a tilt angle θ_T will result between substrate and relaxed film:

$$\theta_{T,i} = \epsilon_{ii} \frac{b_{i,\perp}}{b_{i,\parallel}}, \quad (1.15)$$

where i denotes the axis of strain relaxation. This is schematically depicted in Fig. 1.3.

Slip Systems for Sesquioxide Heterostructures

For heteroepitaxial $(\text{Al}_x\text{Ga}_{1-x})_2\text{O}_3\text{-Al}_2\text{O}_3$ systems with low Al content, studies have been conducted on the prevailing relaxation mechanisms for r -oriented [49, 50], as well as a - and m -oriented [46] growth directions. In the following, those results will be summarized. Note that the x -axis points along the c -axis for m - and a -oriented heterostructures, and similarly along the projection of the c -axis on the sample surface for r -oriented heterostructures.

(01.2)-plane (r -orientation) The two relevant slip systems are $\{00.1\}/\langle 11.0 \rangle$ and $\{11.0\}/\langle 1\bar{1}.1 \rangle$, which contain the “basal” and “prismatic” glide plane, respectively [49]. The former allows relaxation along the direction containing the projection of the c -axis (x -axis), whereas the latter allows relaxation perpendicular to it (y -axis). For the basal system, one can determine two possible independent BURGER’s vectors \mathbf{b}_c with differing screw components but otherwise same tilt and edge components $b_{c,\perp}$ and $b_{c,\parallel}$, respectively. The tilt along x -direction can then be calculated via:

$$\theta_{T,x} = \epsilon_{xx} \frac{b_{c,\perp}}{b_{c,\parallel}} = \frac{1}{\sqrt{3}} \zeta_F \epsilon_{xx}. \quad (1.16)$$

with $\zeta_F = c_F/a_F$. For the prismatic slip system, the possible BURGER’s vectors facilitate relaxation along the y -direction via $b_{a,\parallel}$. But in contrast to the basal system, the tilt components $b_{a,\perp}$ cancel out on average, thus resulting in no net tilt along the y -direction: $\theta_{T,y} = 0$.

(10.0)-plane (m -orientation) Neither basal (00.1) nor prismatic (11.0) and (10.0) slip systems can resolve strain along the x -axis: The (00.1)-plane is perpendicular to the surface and x -direction, thus the BURGER’s vector can only have components in the y - z -plane. But for strain release along x , the BURGER’s vector should have some component

⁽¹⁰⁾ Also referred to as “full” dislocation [47].

in this direction, which cannot be the case. The prismatic planes, on the other hand, are perpendicular to the surface but parallel to the x -axis. This results in a dislocation line along the x -direction. To release strain, the BURGER's vector would have x -component, which does not apply for edge dislocations. So the prevailing slip system must have (01.2)-plane (r -orientation) or (11.2)-plane (s -orientation) character, which are called "pyramidal" slip systems. Three different r -planes contribute to strain release, because there is dislocation line component along the y -axis and BURGER's vector's components along the x -axis. With (1.15) and plugging in the possible BURGER's vectors one finds:

$$\theta_{T,x} = \frac{2}{3} \frac{\sqrt{3}}{\frac{20\zeta}{24+6\zeta^2} + \zeta} \left(\frac{c_S}{c_F} - 1 \right) \quad (1.17)$$

(11.0)-plane (a -orientation) The same argument as for the m -oriented heterostructure holds, why only pyramidal slip systems are possible. But in this case, only two r -planes contribute to strain relaxation, because the third plane is perpendicular to the surface, thus can only exhibit BURGER's vectors without in-plane components which results in no possible edge dislocations. Furthermore, in this case, the BURGER's vectors of the two remaining r -planes have opposite tilt components, i.e. they point outwards and inwards of the surface, respectively. Regarding (1.15), this will result in no net tilt of the thin film.

Chapter 2

Experimental Methods

Contents

2.1 Pulsed Laser Deposition	15
2.1.1 Setup	16
2.1.2 Plasma Dynamics	16
2.1.3 Segmented Target Approach	18
2.2 X-Ray Diffraction Measurement	18
2.2.1 2θ - ω -scans	19
2.2.2 ω -scans	20
2.2.3 φ -scans	20
2.2.4 Reciprocal Space Maps	21
2.2.5 Technical Aspects	23
2.3 Further Methods	24
2.3.1 Thermal Evaporation	24
2.3.2 Resistivity Measurement	25
2.3.3 Thickness Determination	26
2.3.4 Spectral Transmission	27

2.1 Pulsed Laser Deposition

PLD is a Physical Vapor Deposition (PVD) technique, which essentially utilizes absorption of laser energy by a target and subsequent condensation of evaporated target material on a substrate. Like MBE or CVD, it is used for deposition of thin film materials. Although not true in general [51], a stoichiometric transfer of target composition to the substrate is attributed to PLD. In the following, the PLD setup used for this work (Fig. 2.1a) is described. Furthermore, an overview of the basic physical processes interplaying during a PLD process is given, based on Lorenz (2019) [51].

2.1.1 Setup

The desired thin film material is provided by a ceramic pellet of the respective compound called “target”. It is fabricated by pressing powder with high pressure into cylindrical form, before it is sintered at high temperatures. The crystal growth takes place on a substrate, whose material is chosen to be sapphire (Al_2O_3) of different crystal orientation, because it matches the symmetry of the here investigated sesquioxides. These quadratic slabs are $500 \mu\text{m}$ thick with an edge length of 5 mm. In this work, oxygen is chosen as background gas to ensure fabrication of oxide thin film materials. To control the partial pressure of the background gas, the process takes place in a vacuum chamber, called PLD chamber. Inside the chamber, a target holder is placed opposite a sample holder, which both are capable of carrying up to four pellets and substrates, respectively. The latter is equipped with a resistive heater, allowing growth temperatures above 700°C . To ensure homogenous ablation and deposition, both target and substrate can be rotated, whereby a frequency of 60 min^{-1} is chosen in this work. Furthermore, an offset ε between the rotation centers of target and substrate is applied, i.e. the plasma plume does not hit the center of the substrate. To achieve homogeneous thickness distributions of the deposited material, $\varepsilon = 7.5 \text{ mm}$ is chosen. Outside the PLD chamber, a KrF excimer laser produces pulsed radiation, which is redirected by a mirror and enters the chamber through a fused silica window. With a wavelength of 248 nm, a UV lens is needed to project the beam on the target surface, where the laser energy is absorbed. By repositioning the lens, the laser spot size can be controlled. The energy per pulse can be adjusted and is several hundred mJ with a duration of about 20 ns, resulting in thousands of kW cm^{-2} on the target surface [51].

The laser energy density, called fluence F , can be calculated by taking the energy per pulse E and the lens position L into account. For an applied $E = 650 \text{ mJ}$, 75 % of the energy are absorbed by mirror, lens and entrance window. This transmittance is assumed to be independent of E . The resulting fluence dependence $F(E, L) = \frac{0.25E}{A(L)}$ is visualized in Fig. 2.2, whereby the laser spot size A was measured for some L and fitted by assuming parabolic behavior.

2.1.2 Plasma Dynamics

The PLD procedure can be broken down into three physical processes: (i) energy absorption on the target surface, (ii) formation of a plasma and (iii) condensation on the substrate:

- (i) After being projected on the surface of the pellet, the radiation penetrates the material only by a fraction of a μm . Electrons are excited and oscillate in the electromagnetic field of the laser pulse, which is still ongoing. Those electrons collide with bulk atoms of the surface region, which are subsequently heated up and vaporize. This process is supported by breaking of chemical bonds due to laser radiation.
- (ii) A material cloud expands perpendicular to the target surface due to Coulomb repulsion and recoil. Absorption of remaining laser radiation results in a plasma plume which is narrow for low background partial pressures below 10^{-4} mbar . The target is rotated during this process to minimize the deflection of the plasma due

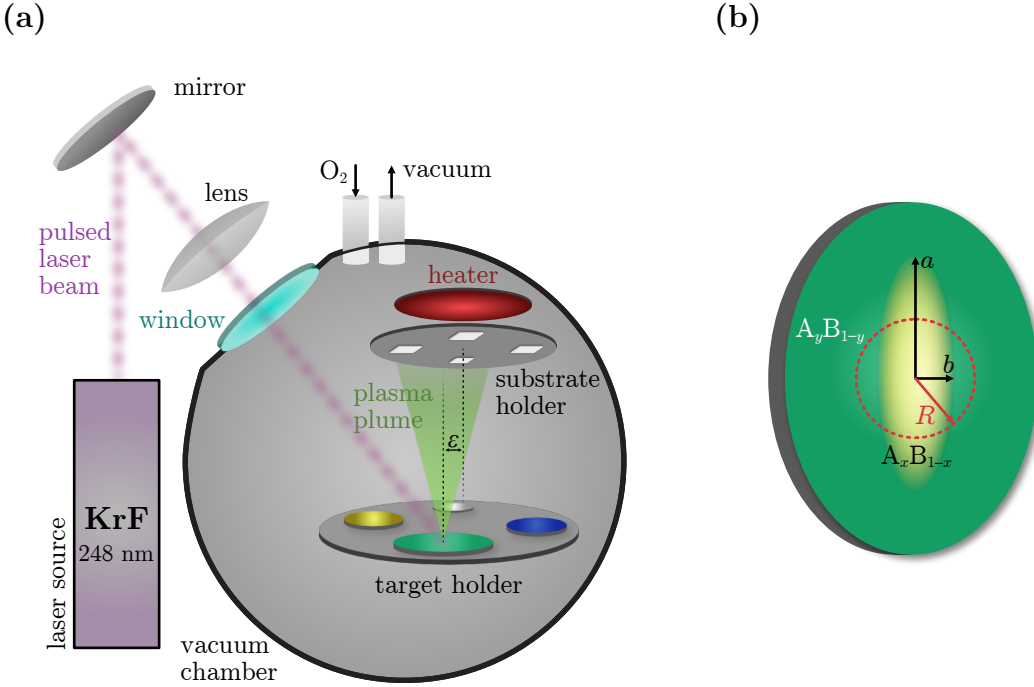


Figure 2.1: (a) Schematic of a PLD setup as described in 2.1.1 (b) Schematic of an elliptically segmented pellet used as target for VCCS-PLD (cf. 2.1.3). a and b are semi-major and semi-minor axis of the ellipse, respectively. R denotes the radius of the circular laser spot path on the target surface. The composition of the inner and outer segment is $A_x B_{1-x}$ and $A_y B_{1-y}$, respectively.

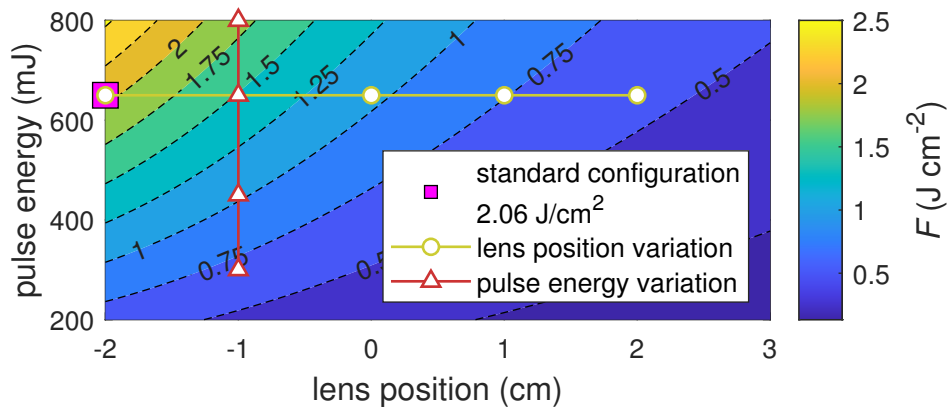


Figure 2.2: Laser energy density depending on the applied pulse energy and lens position. Smaller lens positions yield smaller spot sizes. A value of -2 cm corresponds to the lens being as close as possible to the laser entrance window in the setup used for this work. The default configuration of 650 mJ and -2 cm yields typical fluences of about 2 J cm^{-2} . The triangles and circles represent the variation of laser fluence in this work, achieved by varying the pulse energy and lens position, respectively.

to target degradation. The kinetic energy of the material in the plasma plume is crucial for the deposition process and can be controlled by background partial pressure and laser energy density on the target.

- (iii) The plasma plume hits the substrate which results in resputtering of already deposited material, which condensates together with the plasma, resulting in thermal equilibrium and thus thin film nucleation. A large number of adatoms results in many nucleation centers which is responsible for smooth films.

It becomes clear, that PLD is a non-equilibrium process, making empirical optimization of growth parameters an essential part of thin film manufacturing [51].

2.1.3 Segmented Target Approach

To provide a discrete material library – a set of different samples with homogeneous composition each –, a segmented target approach as described in Wenckstern et al. (2020) [52] is applied. Specifically, the Vertical Continuous Composition Spread (VCCS) method utilizes a segmented target, i.e. a target with distinct regions of different material composition. By varying the laser spot position on the target, different plasma compositions can be achieved. Because the target is rotating during PLD, the material distribution must be in such a way that when the radial position R of the laser on the target changes, the average ablated composition $\chi(R)$ changes. This can be realized with an elliptical segmentation, i.e. a target pellet with overall composition A_yB_{1-y} , but containing an inner ellipse with composition A_xB_{1-x} (Fig. 2.1b). By this means, any homogeneous composition $A_\chi B_{1-\chi}$ with χ between x and y can be realized with only one target. χ is related to the path lengths of the moving laser spot on the inner and outer segment, respectively. The composition in the plasma can be calculated via [52]:

$$\chi(R) = y - (y - x) \frac{2}{\pi} \arccos \left[\frac{1}{\delta} \sqrt{1 - \left(\frac{b}{R} \right)^2} \right] \quad (2.1)$$

where δ and b are eccentricity and semi-minor axis of the ellipse, respectively⁽¹⁾. Small and large R will result in a composition equal to the composition of the inner and outer segment, respectively. To model the process more accurately one has to take into account that the laser does not yield a point-like spot but rather an intensity distribution.

2.2 X-Ray Diffraction Measurement

As described in 1.1.2, constructive interference of incoming and scattered X-rays may give insight in the symmetry of exposed crystal structures. This can be utilized for thin film investigation and is called XRD. The XRD device used for this work, namely an *X’Pert Pro* (*Malvern Panalytical Ltd.*), as well as the applied scanning techniques will be presented in the following.

⁽¹⁾ The eccentricity is defined as $\delta = \sqrt{1 - b^2/a^2}$, where a is the length of the semi-major axis.

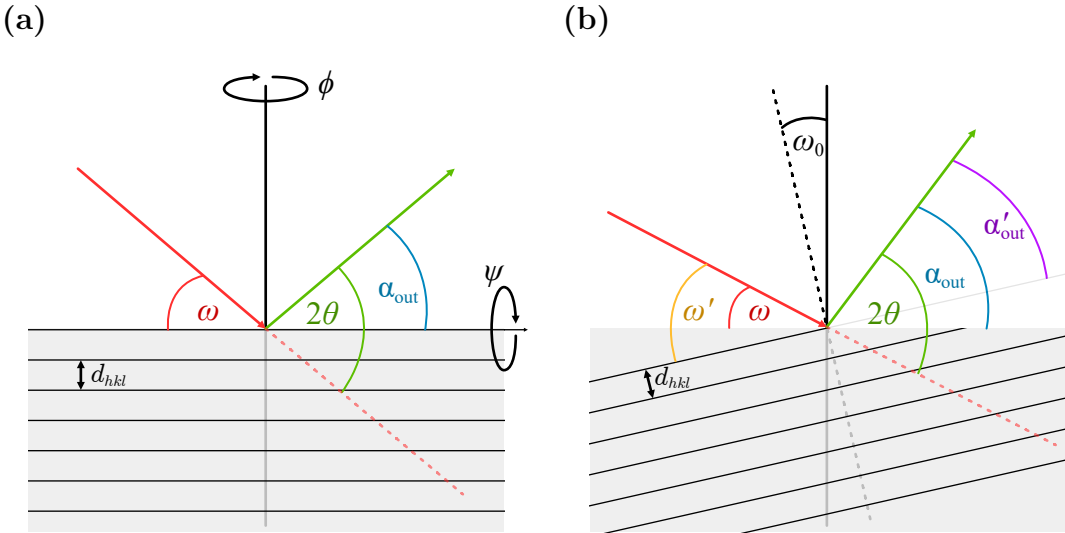


Figure 2.3: (a) Geometry for a 2θ - ω -scan without offset. (b) Scattering geometry containing an offset ω_0 . Angle of incidence and angle of diffraction decrease and increase, respectively. Note that 2θ is not affected by this offset.

A sample with surface normal parallel to the z -axis of the laboratory system is exposed with X-rays at an angle ω between sample surface and incident radiation. The diffracted radiation is measured at an angle α_{out} between sample surface and detector. 2θ is used to describe the angle between outgoing beam and the extension of the incoming beam, which both span the scattering plane. It follows that $2\theta = \omega + \alpha_{\text{out}}$. Note that θ in Equ. (1.9) is the same angle as half of 2θ . The scattering plane is depicted in Fig. 2.3a. The sample can be rotated by ϕ (“azimuth”) and ψ around an axis parallel to the surface normal and parallel to the intersection of sample surface and scattering plane, respectively.

2.2.1 2θ - ω -scans

When probing for lattice plane distances using the BRAGG condition in its simplest form, it is assumed that the scattering planes are parallel to the sample surface (cf. Fig. 2.3a). It is necessary that $\omega = \alpha_{\text{out}}$ which implies $2\theta = 2\omega$. So the angle of incidence ω is coupled to 2θ which represents the distance between lattice planes (cf. Equ. (1.9)). Measuring the diffracted X-ray intensity while varying 2θ and maintaining the condition $2\theta = 2\omega$, is called a 2θ - ω -scan. This results in a so-called 2θ - ω diffraction pattern, where peaks correspond to constructive interference and thus to certain lattice plane distances.

When analyzing 2θ - ω diffraction patterns, one usually compares to predicted peak positions of the expected phase of the compound which is investigated. This reference diffraction pattern stems from powder samples of the respective compound, containing all crystal orientations during one 2θ - ω -scan. When a peak is identified, a possible peak shift is determined and the shape of the peak is investigated. Peak shifts may be due to residual stress, substrate induced strain or compositional gradients in the thin film [2]. A minimum amount of peak broadening is always present due to convergence of

the incident beam as well as convolution of $K\alpha_1$ - and $K\alpha_2$ -radiation (cf. 1.1.2), which is called instrumental broadening [2]. The Full Width at Half Maximum (FWHM) of the highly crystalline substrate peaks may give a reference for broadening of peaks in $2\theta\text{-}\omega$ diffraction data.

This method can be extended to measure lattice planes which are not parallel to the sample surface but tilted by ω_0 . This is done by rotating the reference frame of the sample in such a way that the BRAGG condition is fulfilled again. Note that 2θ does not change upon rotation, as can be seen in Fig. 2.3b. When probing for plane distances of the rotated lattice, one finds for the coupling between 2θ and ω :

$$\begin{aligned}\omega' &= \alpha'_{\text{out}} \\ \omega + \omega_0 &= \alpha_{\text{out}} - \omega_0 \\ \omega + \omega_0 &= (2\theta - \omega) - \omega_0 \\ \Rightarrow 2\theta &= 2(\omega + \omega_0) = 2\omega'.\end{aligned}$$

This coupling is equivalent to a $2\theta\text{-}\omega$ -scan but with an offset ω_0 applied to the angle of incidence. There are several use cases for applying an offset ω_0 :

- (i) It is assumed that ω denotes the angle between incident X-ray beam and the sample surface. But a perfect alignment between sample and sample holder is not always possible. So to correct this tilt between expected sample position and its real inclination, the offset ω_0 can be set to really probe for lattice planes parallel to the sample surface. This is done before measuring a $2\theta\text{-}\omega$ -scan to achieve preciser results.
- (ii) When probing for lattice planes which are not parallel to the sample surface (“asymmetric reflections”), one can apply the expected inclination angle as an offset ω_0 . This is the case in Fig. 2.3b.
- (iii) When 2θ is fixed, but ω_0 is varied, a so-called ω -scan is performed, which enables quantification of mosaicity (cf. 2.2.2).

2.2.2 ω -scans

Thin films may exhibit a distribution of lattice plane inclination, called mosaicity. This results in an observation of diffraction peaks for several offsets ω_0 . The mosaicity can thus be quantified by fixing 2θ , representing a certain lattice plane distance, and then vary ω_0 and measure the X-ray intensity. This is called an ω -scan, and the FWHM of the observed diffraction pattern (also called “Rocking curve”) is a measure for the mosaicity [2]. ω -scans are particularly useful when comparing a set of thin films of varying deposition parameters to optimise growth conditions. In particular, recording Rocking curves of symmetric and asymmetric lattice planes allows the calculation of dislocation densities in the thin film [53].

2.2.3 φ -scans

A $2\theta\text{-}\omega$ -scan is not capable of resolving in-plane rotations of crystal domains, because the distance of lattice planes parallel to the surface are not affected. Those rotational

domains can be detected by probing for lattice planes which are inclined with respect to the surface, i.e. by fixing 2θ to the expected lattice plane distance and ω_0 to the inclination angle (cf. Fig. 2.3b). Depending on the symmetry of the inspected material, constructive interference should only appear for distinct values of ϕ . So by rotating the sample by 360° and simultaneously recording the X-ray intensity, a so-called φ -scan (also called “Azimuth-scan”) can yield information about the existence of rotational domains. If the number of observed peaks in the φ -scan diffraction pattern exceeds the theoretically expected number for a single crystal, rotational domains are present [2]. Furthermore, comparing the φ -scan diffraction data of thin film and substrate reveals whether the film has grown with an in-plane rotation with respect to the substrate. Finally, if the thin film grows in a tilted manner on the substrate, a φ -scan prior to an ω -scan can ensure the correct positioning before alignment. Then, the BRAGG condition is fulfilled for performing a 2θ - ω -scan.

2.2.4 Reciprocal Space Maps

Because the BRAGG condition is equal to the description of diffraction with $\mathbf{k}' - \mathbf{k}$ and reciprocal space vectors \mathbf{K}_{hkl} (cf. 1.1.2), both can be used depending on context. Henceforth, $\mathbf{k}' - \mathbf{k}$ will be denoted by the “scattering vector” \mathbf{q} . Note that \mathbf{k} and \mathbf{k}' are parallel to incoming and outgoing beam, respectively. From the definition of angles, it follows that

$$\mathbf{q} = \begin{pmatrix} q_{\parallel} \\ q_{\perp} \end{pmatrix} = \mathbf{k}' - \mathbf{k} \quad (2.2)$$

$$= \frac{1}{\lambda} \begin{pmatrix} \cos \alpha_{\text{out}} \\ \sin \alpha_{\text{out}} \end{pmatrix} - \frac{1}{\lambda} \begin{pmatrix} \cos \omega \\ -\sin \omega \end{pmatrix} \quad (2.3)$$

$$= \frac{1}{\lambda} \begin{pmatrix} \cos(2\theta - \omega) - \cos(\omega) \\ \sin(2\theta - \omega) + \sin(\omega) \end{pmatrix}. \quad (2.4)$$

From Equ. (2.4), two properties follow for the scattering vector:

$$-q_{\parallel}/q_{\perp} = -\tan \left(\omega - \frac{2\theta}{2} \right) = \tan \omega_0, \quad (2.5)$$

$$|\mathbf{q}| = \sqrt{q_{\parallel}^2 + q_{\perp}^2} = \frac{1}{\lambda} 2 \sin \theta \stackrel{\text{Bragg}}{=} \frac{1}{d_{hkl}}, \quad (2.6)$$

where the last equality of Equ. (2.6) holds, if \mathbf{q} is a reciprocal lattice vector \mathbf{K}_{hkl} . The scattering vector, together with the corresponding XRD geometry is depicted in Fig. 2.4a. Because 2θ and ω can simultaneously be represented by \mathbf{q} , it is possible to measure intensities for several \mathbf{q} , such that a part of the reciprocal space $Q \ni \mathbf{q}$ is mapped. Consequently, this is called a Reciprocal Space Map (RSM). According to Equ. (1.8), a peak in 2D reciprocal space Q should be observed if \mathbf{q} is a reciprocal space vector. In this case, $\mathbf{q} = \mathbf{K}_{hkl}$ is called a “reflection”. With Equ. (2.5) one can determine ω_0 – the direction of the corresponding lattice planes⁽²⁾, and with Equ. (2.6) the lattice

⁽²⁾ Note that the “–” in $-q_{\parallel}/q_{\perp}$ is necessary, such that this fraction is the tangens the angle between \mathbf{q} and surface normal with correct sense of rotation.

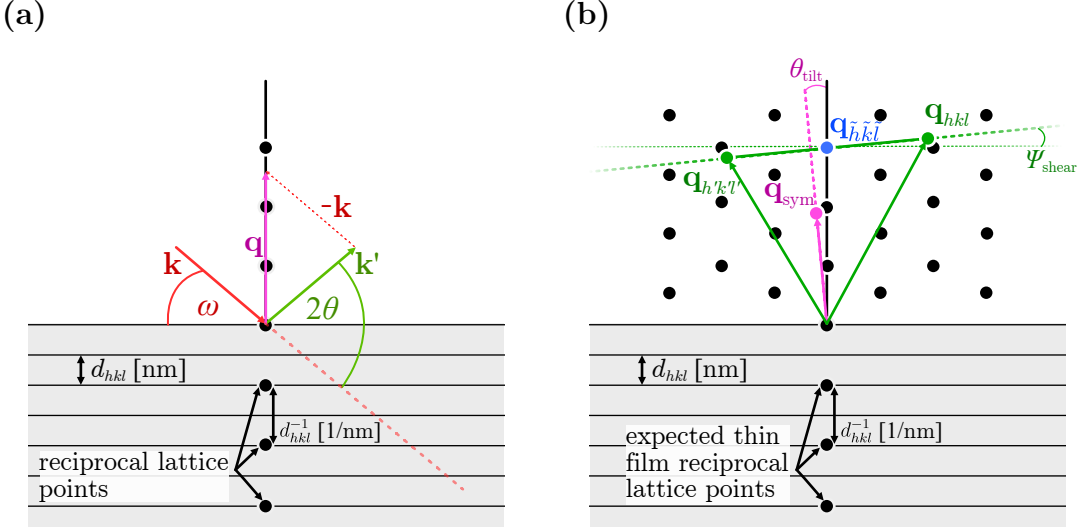


Figure 2.4: (a) Construction of the scattering vector (magenta) from incoming (red) and outgoing (green) beam, according to Eq. (2.4). The reciprocal lattice points are visualized together with the lattice planes. It has to be noted that the distances between lattice planes and between reciprocal lattice points have different dimensions. (b) *tbd*

plane distance d_{hkl} can be calculated. Note that for rhombohedral crystals, d_{hkl} can also be predicted from the lattice constants a and c with the following equation [43]:

$$d_{hkl} = \left(\frac{4}{3} \frac{h^2 + k^2 + hk}{a^2} + \frac{l^2}{c^2} \right)^{-1/2}. \quad (2.7)$$

The inclination with respect to the c -axis can be determined via [49]

$$\alpha_{hkl|c} \arccos \left(\frac{l}{\sqrt{\frac{4c^2}{3} \frac{h^2+k^2+hk}{a^2} + l^2}} \right). \quad (2.8)$$

A 2θ - ω -scan corresponds to a set of \mathbf{q} with fixed direction in reciprocal space, but varying length. For scanning symmetric reflections, \mathbf{q} is parallel to the surface normal (as in Fig. 2.4a). On the other hand, an ω -scan corresponds to a set \mathbf{q} with fixed length but varying direction. The mosaicity can therefore approximately quantified by the broadening of a reflection perpendicular to the direction of \mathbf{K}_{hkl} . Because anisotropic strain has an effect on direction and length of inclined lattice planes, asymmetric reflections, i.e. $\omega_0 \neq 0$, can be deconvoluted into an in-plane and out-of-plane component. By this means, RSMs enable the calculation of lattice constants. To precisely calculate the latter, several corrections are applied to the recorded RSMs, as proposed in Kneiß et al. (2021) [46]:

1. High-quality sapphire substrates are used for deposition of thin films. It can be assumed that they have the expected crystal structure of bulk α -Al₂O₃ (cf. Tab. 1.1). So any deviation of the observed reflection $\mathbf{q}_{hkl}^{\text{Al}_2\text{O}_3,\text{obs}}$ from the expected peak position $\mathbf{q}_{hkl}^{\text{Al}_2\text{O}_3,\text{lit}}$ is corrected by a rotation \mathbf{R} and scaling ρ of reciprocal space Q :

$$\mathbf{q}^{\text{cor}} = \rho \mathbf{R} \cdot \mathbf{q}^{\text{obs}} \quad , \quad \mathbf{q}^{\text{obs}} \in Q, \quad (2.9)$$

with

$$\mathbf{R} = \begin{pmatrix} \cos \gamma & -\sin \gamma \\ \sin \gamma & \cos \gamma \end{pmatrix}, \quad \gamma = \arccos \left(\frac{\mathbf{q}_{hkl}^{\text{Al}_2\text{O}_3,\text{lit}} \cdot \mathbf{q}_{hkl}^{\text{Al}_2\text{O}_3,\text{obs}}}{|\mathbf{q}_{hkl}^{\text{Al}_2\text{O}_3,\text{lit}}| \cdot |\mathbf{q}_{hkl}^{\text{Al}_2\text{O}_3,\text{obs}}|} \right) \quad (2.10)$$

$$\rho = \frac{|\mathbf{q}_{hkl}^{\text{Al}_2\text{O}_3,\text{lit}}|}{|\mathbf{q}_{hkl}^{\text{Al}_2\text{O}_3,\text{obs}}|}. \quad (2.11)$$

2. If the thin film grows tilted (e.g. due to slip systems, cf. 1.3.2), a symmetric reflection – having scattering vector parallel to the surface normal in theory – will exhibit an in-plane component $q_{\parallel,hkl}^{\text{film}} \neq 0$. The tilt angle can be calculated by Equ. (2.5):

$$\theta_{\text{tilt}} = \arctan \left(-\frac{q_{\parallel,hkl}^{\text{film}}}{q_{\perp,hkl}^{\text{film}}} \right). \quad (2.12)$$

To determine the lattice constants from asymmetric peaks, the reciprocal space is again rotated as in Equ. (2.10) but with rotation angle $-\theta_{\text{tilt}}$. This scenario is depicted in Fig. 2.4b, where the magenta colored reflection deviates from the expected symmetric position.

3. If the thin film is sheared, a symmetric reflection $\mathbf{q}_{\tilde{h}\tilde{k}\tilde{l}}^{\text{film}}$ will be unaffected. On the contrary, an asymmetric reflection with both in- and out-of-plane component is affected. To get reliable results for the lattice constants, this shear angle Ψ_{shear} has also to be corrected, and can be calculated from two inclined lattice planes (hkl) and ($h'k'l'$), i.e. scattering vectors with non-zero in-plane component. Those vectors must have symmetry of a mirror plane perpendicular to the scattering plane⁽³⁾. The geometry is depicted in Fig. 2.4b, with the blue and green reflections representing the symmetric and asymmetric reflections, respectively. The shear angle can be calculated with

$$\Psi_{\text{shear}} = \arctan \left(\frac{q_{\perp,hkl}^{\text{film}} - q_{\perp,h'k'l'}^{\text{film}}}{q_{\parallel,hkl}^{\text{film}} - q_{\parallel,h'k'l'}^{\text{film}}} \right). \quad (2.13)$$

To correct the shear, a rotation around the corresponding symmetric reciprocal lattice point $\mathbf{q}_{hkl}^{\text{film}}$ with the same expected out-of-plane component must be applied.

2.2.5 Technical Aspects

The radiation is produced by an copper anode, resulting in a wavelength of $\lambda = 1.5406 \text{ \AA}$ for Cu-K α_1 radiation. Note that Cu-K α_2 and Cu-K β radiation is not filtered out, resulting in additional low-intensity peaks in the diffractograms. Furthermore, contamination of the anode with tungsten results in an observable W-L α_1 contribution with energy between Cu-K α - and Cu-K β -radiation. During the course of the conducted experiments, the contaminated anode has been replaced, so the peaks corresponding to W-L α_1 -radiation are not present in every diffractogram.

⁽³⁾ This can be achieved by probing for a plane (hkl) and then rotate the sample around ϕ by 180° .

Table 2.1: Configurations for the applied XRD scans.

scan type	detector mode	step size ($^{\circ}$)	active channels	effective width
2 θ - ω -scan	1D Scanning Line	0.005	255	2.51 $^{\circ}$
ω -scan	0D Receiving Slit	0.005	55	3.025 mm
ω -optimization	0D Receiving Slit	0.02	37	2.035 mm
φ -scan	0D Receiving Slit	0.05	55	3.025 mm
φ -optimization	0D Receiving Slit	0.5	55	3.025 mm
RSMs	1D Frame Based	0.005	255	2.51 $^{\circ}$

The diffracted radiation is detected with a *PIXcel^{3D}* (*Malvern Panalytical Ltd.*) detector. For 2 θ - ω -scans (cf. 2.2.1), the detector is operating in “Scanning Line” mode. For scans fixing the 2 θ position, i.e. ω - (cf. 2.2.2) and φ -scans (cf. 2.2.3), the detector is operated in “Receiving Slit” mode. RSMs are recorded with the “Frame Based” mode. The settings for the various scans are listed in Tab. 2.1. Note that it is distinguished between scans and optimizations. The latter were applied for aligning the sample correctly, depending on the measurement. For example, before a 2 θ - ω -scan of m -plane oriented rhombohedral samples, a φ -scan has been applied for the inclined (30.6) reflection to find the correct azimuth of the c -axis, which is called φ -optimization. Afterwards, a Rocking curve has been recorded and ω set to the maximum of the peak to compensate for the expected lattice tilt (cf. 1.3.2), called an ω -optimization.

2.3 Further Methods

2.3.1 Thermal Evaporation

The ohmic contacts for electrical characterization of Cr₂O₃ thin films were deposited by means of thermal evaporation. This method was already utilized for successfully contacting α -Ga₂O₃ thin films [54], thus also applied for similarly structured Cr₂O₃ thin films. This PVD method utilizes a “boat” made of a material with high melting temperature (tungsten W or molybdenum Mo) that is loaded with the target material in form of powder or filament. A vacuum chamber is used to achieve pressures of around 5×10^{-5} mbar. A high current is driven through the contacted boat, such that resistive heating ensures melting of the target material and subsequent evaporation. The evaporated material spreads out due to the pressure gradient and condensates on the sample which is mounted to a rotating holder. A metal mask ensures that only the corners of the sample are contacted.

The contacts are either a stacking of titanium, aluminum, and gold (“Ti-Al-Au”) or only titanium and gold (“Ti-Au”). The thickness of each material layer is around 30 nm, measured with a crystal oscillator during the process. The currents used for evaporating Ti, Al and Au are 60 A, 50 A and 45 A, respectively.

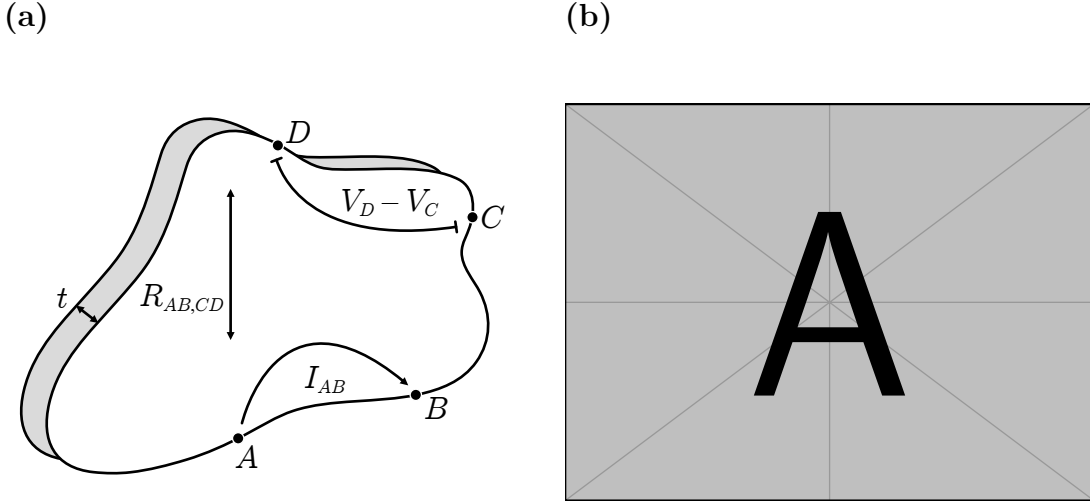


Figure 2.5: (a) The geometry for measuring the specific resistance as proposed by Pauw (1958) [55]. (b) Image of a 5 mm × 5 mm sample, contacted for resistivity measurements.
tbd

2.3.2 Resistivity Measurement

As shown by Pauw (1958) [55], it is possible to determine the specific resistivity of a flat sample by only making four small contacts at arbitrary points at its edge and measure the thickness t as well as the following resistances:

$$R_{AB,CD} = \frac{V_D - V_C}{I_{AB}} \quad , \quad R_{BC,DA} = \frac{V_A - V_D}{I_{BC}} , \quad (2.14)$$

where $V_D - V_C$ is the potential difference between points C and D , measured while applying I_{AB} , the current entering the sample at point A and leaving it at point B . The geometry⁽⁴⁾ is depicted in Fig. 2.5a. The specific resistivity ρ can then be calculated via

$$\rho = \frac{\pi t}{\ln 2} \frac{R_{AB,CD} + R_{BC,DA}}{2} \cdot f \left(\frac{R_{AB,CD}}{R_{BC,DA}} \right) , \quad (2.15)$$

where f is a function equal to 1, if the two measured resistances are equal; f decreases for higher ratios of the two measured resistances [55]. The geometry can further be used to determine the Hall mobility μ_H and carrier concentration n , but due to low conductivities of the here investigated Cr₂O₃ thin films, this method yields no reliable information about μ_H and n .

Temperature-dependent resistivity measurements are conducted with a Hall probe station *CRX-VF* controlled by the measurement setup *HM-8425* (Lake Shore Cryotronics, Inc.), cooled via a *Model 336 cryogenic temperature controller* (Lake Shore). The samples are measured in a vacuum and the temperature can be controlled between 10 K and 390 K.

⁽⁴⁾ Note that Equ. 2.15 is restricted to these conditions: “(a) The contacts are at the circumference of the sample. (b) The contacts are sufficiently small. (c) The sample is homogeneous in thickness. (d) The surface of the sample is singly connected, i.e., the sample does not have isolated holes.” (Pauw (1958) [55])

2.3.3 Thickness Determination

The optical constants and thickness t of a thin film can be measured by the change of polarization state upon light reflection. If the probing light covers several wavelengths at once, one refers to spectroscopic ellipsometry, which will be presented in the following, based on Fujiwara (2007) [56]. The incoming light can be represented by an electromagnetic wave, decomposed into two components being parallel (p) and perpendicular (s) to the scattering plane:

$$\mathcal{E} = \mathcal{E}_{\text{ip}} + \mathcal{E}_{\text{is}}. \quad (2.16)$$

In general, the amplitudes of p- and s-polarized light change in a different manner after reflection, so the overall polarization of the reflected light is changed. This change is described by the fraction

$$\rho = \frac{r_p}{r_s} := \tan \Psi \cdot \exp(i\Delta), \quad (2.17)$$

where r_p and r_s are the amplitude reflection coefficients⁽⁵⁾ for the p- and s-polarized component, respectively. For simple structures, Ψ is essentially the refractive index n , and Δ represents the extinction coefficient k . In general, they can be calculated from the JONES-matrix – representing the reflection – and depend on the angle of incidence as well as the photon energy.

To determine the sample thickness, the spectra of Ψ and Δ can be generated using a model for the sample structure, which is then fitted to the experimental data. In this work, this model consists of an Al_2O_3 substrate without backscattering from the backside (infinite thickness); a Cr_2O_3 thin film of thickness t ; and a mixed layer of air and Cr_2O_3 , approximating the roughness of the sample. Because the measured spectra were confined to the visible regime of the thin film (approx. < 2.8 eV), one can apply the CAUCHY model [56], approximating the refractive index by

$$n(\lambda) = A + \frac{B}{\lambda^2} + \frac{C}{\lambda^4} + \mathcal{O}(\lambda^{-6}) \quad , \quad k = 0. \quad (2.18)$$

The spectroscopic ellipsometry measurements are done with an *M-2000VI* (J.A. Woolam Co., Inc.) and the data is analyzed using the software *WVASE* (J.A. Woolam). The angles of incidence are chosen to be 50° , 60° and 70° , and the modelled spectral range is 0.75 to 2.8 eV. If samples of different orientation were fabricated in the same process, one can assume similar thicknesses, and a measurement with three angles was conducted only for one sample of the batch. The other samples were measured with only one angle, if the determined thickness did not differ significantly from the more accurately measured one.

Note that the investigated thin films are not isotropic in general, which is why the validity of the determined thickness is checked by profilometer measurements with a *Dektak XT Stylus Profiler* (Bruker Corporation). The edges of the quadratic substrates are masked by the sample holder during deposition, which is why they are not deposited with the target material. Consequently, measuring the height profile ranging from an edge to coated regions of the sample yields an approximation for t by the height of the observed step edge.

⁽⁵⁾ They are defined by the amplitude of incoming (i) and reflected (r) radiation: $r = |\mathcal{E}_r|/|\mathcal{E}_i|$.

2.3.4 Spectral Transmission

tbd

Chapter 3

Experiment, Results and Discussion

Contents

3.1	Preliminary Investigations	29
3.1.1	Experiment	29
3.1.2	Results	30
3.1.3	Conclusion	38
3.2	Doping of Cr₂O₃ Thin Films	40
3.2.1	Experiment	40
3.2.2	Results	41
3.2.3	Conclusion	48
3.3	Strain Analysis	50
3.3.1	Experiment	50
3.3.2	Results	53

3.1 Preliminary Investigations

In the following, the feasibility of depositing Cr₂O₃ thin films via PLD as well as their resulting properties are investigated. Since α -Cr₂O₃ is the only phase of chromia (cf. 1.2.1), it is expected that the growth results in either rhombohedral or amorphous films. Furthermore, if a crystalline phase is present, the orientation with respect to the sapphire substrates is of interest. Because Al₂O₃ and Cr₂O₃ exhibit the same crystal symmetry, it is expected that the crystal orientation of the film matches the corresponding substrate orientation. Finally, deposition parameters should be optimized to obtain the best crystal quality.

3.1.1 Experiment

Due to the similar crystal structure of Cr₂O₃ and α -Ga₂O₃, the deposition parameters of the latter were chosen as a starting point to deposit chromia thin films on 10 × 10 mm² sapphire substrates with *m*-plane orientation. Namely, a pulse energy of 650 mJ and

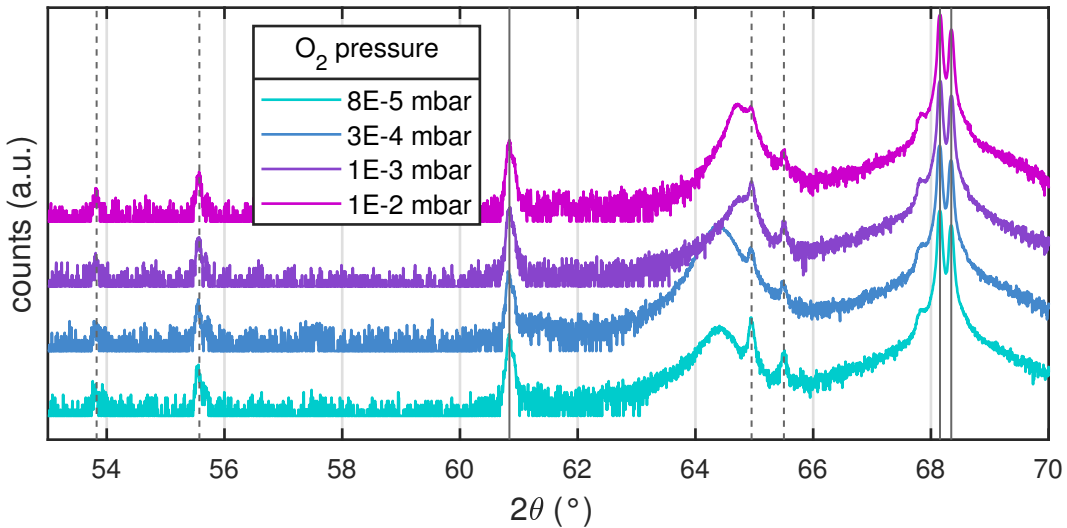


Figure 3.1: $2\theta\text{-}\omega$ -patterns of Cr_2O_3 thin films deposited on *m*-plane sapphire for various oxygen partial pressures. The solid lines indicate (30.0) substrate reflections corresponding to copper radiation, whereas the dashed lines indicate (30.0) substrate reflections corresponding to tungsten radiation.

a pulse frequency of 20 Hz were applied for a total of 30 000 pulses. To investigate the influence of deposition parameters, three batches were produced:

1. variation of oxygen partial pressure from 8×10^{-5} to 1×10^{-2} mbar with a fixed temperature of 745°C ,
2. variation of growth temperature from 725 to 765°C with a fixed oxygen partial pressure of 1×10^{-3} mbar, and
3. variation of substrate orientation between *c*- (00.1), *r*- (01.2) *m*- (10.0) and *a*-plane (11.0) $5 \times 5 \text{ mm}^2$ sapphire substrates⁽¹⁾ with a fixed oxygen partial pressure of 1×10^{-3} mbar and a growth temperature of 715°C .

Structural properties of those thin films were determined by $2\theta\text{-}\omega$ -scans, ω -scans and φ -scans. The thickness was determined via spectroscopic ellipsometry, and transmission spectra were recorded for two samples of the 1st batch to determine the optical band gap. Temperature dependent resistivity measurements were performed only for the samples of the 3rd batch, because all *m*-plane oriented samples showed no conductivity at room temperature.

3.1.2 Results

Oxygen Partial Pressure Variation on *m*-plane Sapphire

In the following, the results for the samples produced at four different oxygen partial pressures are analyzed. In Fig. 3.1, the $2\theta\text{-}\omega$ -patterns are depicted. For each pattern, the two peaks (solid line) at around 68° correspond to the (30.0) reflection of the *m*-plane oriented sapphire substrate. The splitting occurs due to the similar wavelength of

⁽¹⁾ In the following, the BRAVAIS-MILLER-indices will be omitted.

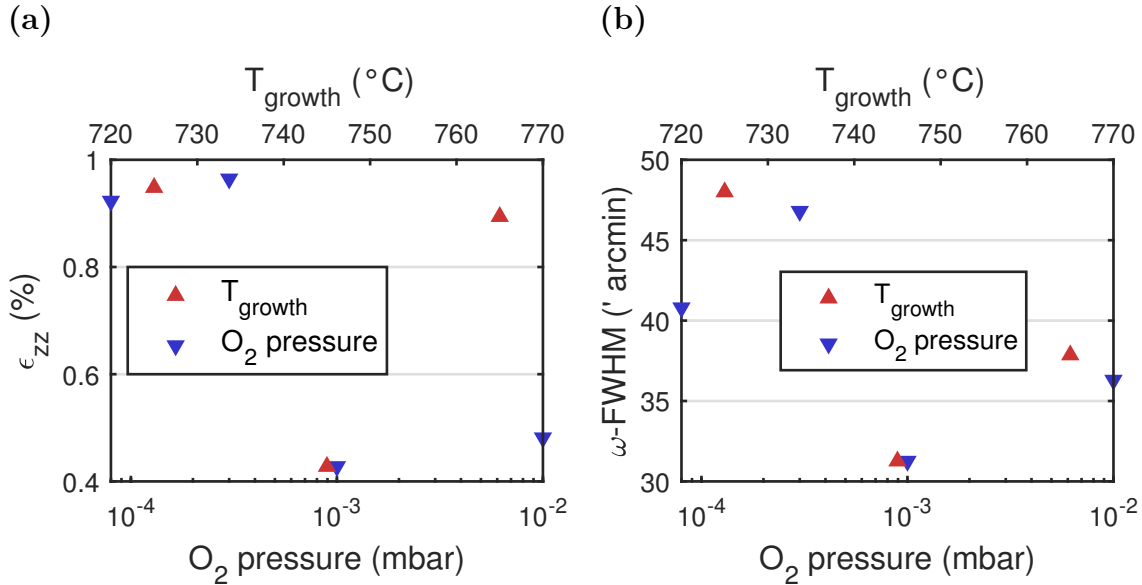


Figure 3.2: (a) o.o.p. strain calculated with Equ. 3.1 and (b) ω -FWHMs for samples from growth temperature series (red triangles, top x -axis) and oxygen partial pressure series (blue triangles, bottom x -axis).

Cu-K α_1 and Cu-K α_2 radiation. The additional peaks also stem mainly from the (30.0) reflection of Al₂O₃ and are caused by W-L β_2 -, W-L β_1 -, Cu-K β -, W-L α_1 - and W-L α_2 -radiation (increasing angles).⁽²⁾ In the vicinity of the calculated peak position for the (30.0) reflection of Cr₂O₃ (cf. 1.3), there is a peak observed for each sample, indicating that the α -phase of Cr₂O₃ is present. Note that the peak position is varying depending on the chosen oxygen partial pressure. The difference to the expected peak position $2\theta_0$ is expressed as o.o.p. strain ϵ_{zz} using the Bragg equation Equ. 1.9 and then

$$\epsilon_{zz} = \frac{d - d_0}{d_0} = \left(\frac{1}{\sin(2\theta/2)} - \frac{1}{\sin(2\theta_0/2)} \right) \cdot \sin(2\theta_0/2). \quad (3.1)$$

In Fig. 3.2a, the calculated strain is shown in dependence of the corresponding oxygen partial pressure. The strain decreases from approx. 0.95 % to 0.45 % with increasing pressure. This strain reduction may therefore be the result of increased background gas scattering which results in less kinetic energy of the specimen reaching the heated substrate (cf. 2.1.1).

For each sample, the 2θ angle was fixed to the observed (30.0) reflection of Cr₂O₃ and an ω -scan was performed. The FWHM of the ω -patterns (henceforth “ ω -FWHM”) are depicted in Fig. 3.2b. The values vary between approx. 30' and 50' and show a dependence on oxygen partial pressure, which is less pronounced compared with o.o.p. strain (Fig. 3.2a). Still, since ω -FWHM is connected to the mosaicity of the thin film, higher oxygen partial pressures yield slightly better crystal qualities. Note that due to the fact that an oxygen partial pressure of 1×10^{-3} mbar yielded the best crystal quality, this value is used for future deposition processes.

To probe for rotational domains of the thin films, φ -scans were performed by fixing 2θ and ω to the corresponding angles of the (30.6) plane of Cr₂O₃, which has an inclination

⁽²⁾ Klar wäre das besser das im plot an die linien zu schreiben, aber das war mir irgendwie zu auffällig es schön zu machen. Gehts auch so?

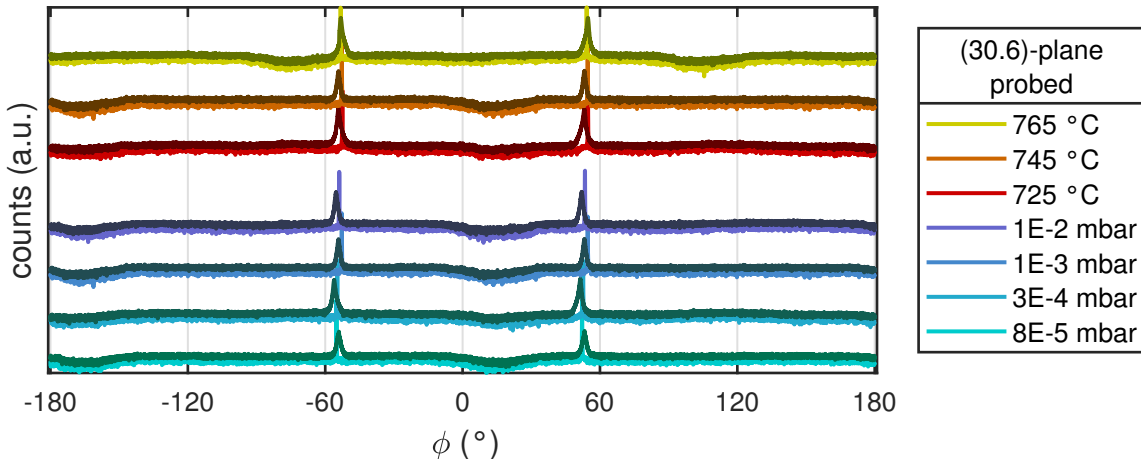


Figure 3.3: Diffraction patterns of φ -scans performed on the inclined (30.6) reflections for m -plane Cr_2O_3 (darker color) and Al_2O_3 (brighter color). The diffraction patterns cover the samples from variation of oxygen partial pressure (teal to blue colored) and variation of growth temperature (red to yellow colored).

angle of 32.4° with respect to the (30.0) plane. The diffraction patterns are depicted in Fig. 3.3. The observed peaks of the thin film align with the peaks of the single crystal substrate, indicating that the film has no in-plane rotation with respect to the substrate. Furthermore, the absence of additional peaks indicates that there exists only a single domain of the thin film⁽³⁾.

The growth rate g varies between 3 pm pulse^{-1} and 7 pm pulse^{-1} and is depicted in Fig. 3.4a. No systematic dependence on the oxygen partial pressure can be observed.

The transmission spectra of two selected Cr_2O_3 thin films are shown in Fig. 3.5a. The samples are not fully transparent in the visible spectrum and they exhibit a greenish tint, as can also be seen in Fig. 3.4b. To determine the onset of absorption E_τ , a Tauc-plot (Fig. 3.5b) is utilized (cf. 2.3.4). The exponent is chosen to be $\frac{1}{2}$, resulting in a representation of $(\alpha E)^2$ vs. E . Although the publications used for reference in this work support the direct transition nature of Cr_2O_3 [13, 25], it has to be noted that there exist studies determining the optical band gap of Cr_2O_3 by applying an exponent of 2, assuming an indirect band gap transition for Cr_2O_3 [11, 15]. Fitting the linear regime in the onset of absorption results in $E_\tau \approx 3.7 \text{ eV}$ for both samples, which differ in strain and ω -FWHM by a factor of approx. 2 and 0.3, respectively.

Growth Temperature Variation on m -plane Sapphire

In the following, the results for the three samples produced at different growth temperatures are presented. Similar to the previous results, the (30.0) reflection of the α -phase of Cr_2O_3 can be observed (Fig. 3.6). Note that the additional peaks are corresponding to the (30.0) reflection of the substrate and stem from various radiation wavelengths. The calculated o.o.p. strain is shown in Fig. 3.2a and a large spread of strain can be observed, varying between 0.4 % and 1 %. Note that there is no systematic dependence

⁽³⁾ Vielleicht müsste ich noch erwähnen warum die beiden Reflections hier bei $+55^\circ$ und -55° liegen, also 110° auseinander. Aber das versteh ich selber nicht so richtig :(ich würde erwarten dass sie 180° auseinander liegen.

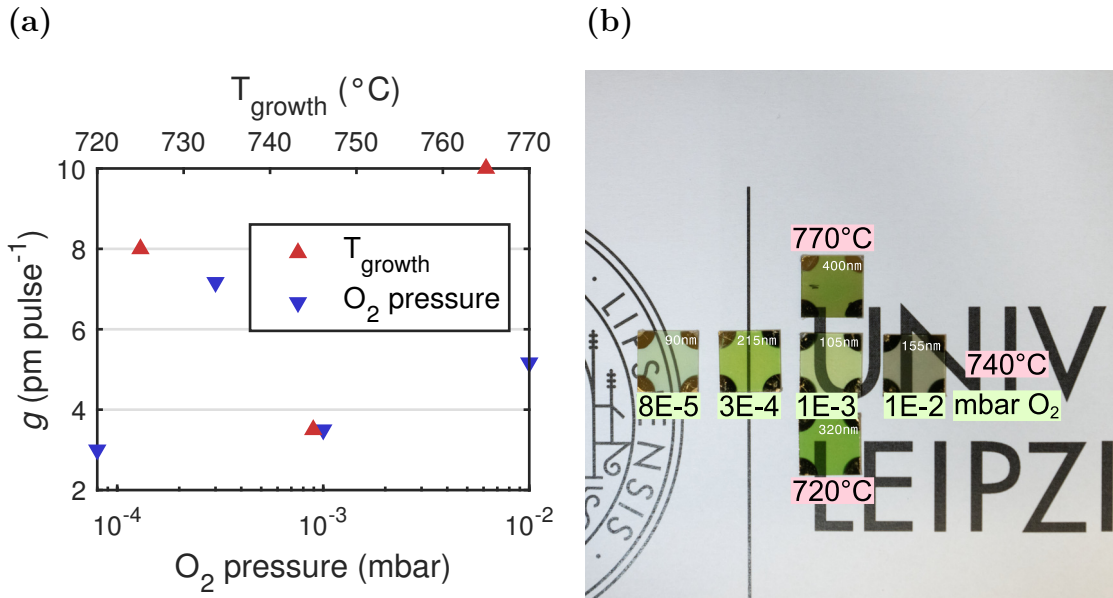


Figure 3.4: (a) Growth rates g for samples from growth temperature series (red triangles, top x -axis) and oxygen partial pressure series (blue triangles, bottom x -axis). (b) Image of the samples produced at different oxygen partial pressures and different growth temperatures.

on growth temperature. The ω -FWHMs of the Cr₂O₃ (30.0) reflection are shown in Fig. 3.2b and exhibit a similar spread as the samples with varying oxygen partial pressure, but similar to the o.o.p. strain, no dependence on growth temperature is observed. The φ -scans (Fig. 3.3) show that the thin films are in-plane aligned with the respective substrate and that no rotational domains are present. Finally, the growth rate varies between 3.5 pm pulse $^{-1}$ and 10 pm pulse $^{-1}$ with no observable dependence on growth temperature.

Influence of Growth Rate on Crystal Structure

It has to be noted that there is a large spread in strain and ω -FWHM for the samples that were deposited at different growth temperatures. The range of temperature variation was only 40 °C and has no significant influence on the distribution of strain and ω -FWHM (Fig. 3.2). Because all the other process parameters were kept the same⁽⁴⁾, this indicates that another parameter influences the crystal quality. This is supported by the fact that the growth rate correlates with the magnitude of strain and ω -FWHM, as can be seen in Fig. 3.7a. Although strain is related to ω -FWHM, it has to be noted that for a small regime of o.o.p. strain around approx. 0.9 %, the ω -FWHM scatters between approx. 37' and 47'.

The origin of the varying growth rate – and therefore varying crystal quality – can be found when taking the number of processes into account that were performed before. In Fig. 3.7b, the growth rate is visualized depending on the order of sample fabrication. It is also indicated when the laser entrance window has been cleaned. It is common

⁽⁴⁾ In fact, for the last two samples produced ($\Theta = 725$ °C and $\Theta = 765$ °C), the pulse number was increased to 40 000 pulses. This was due to the fact that the growthrate decreased.

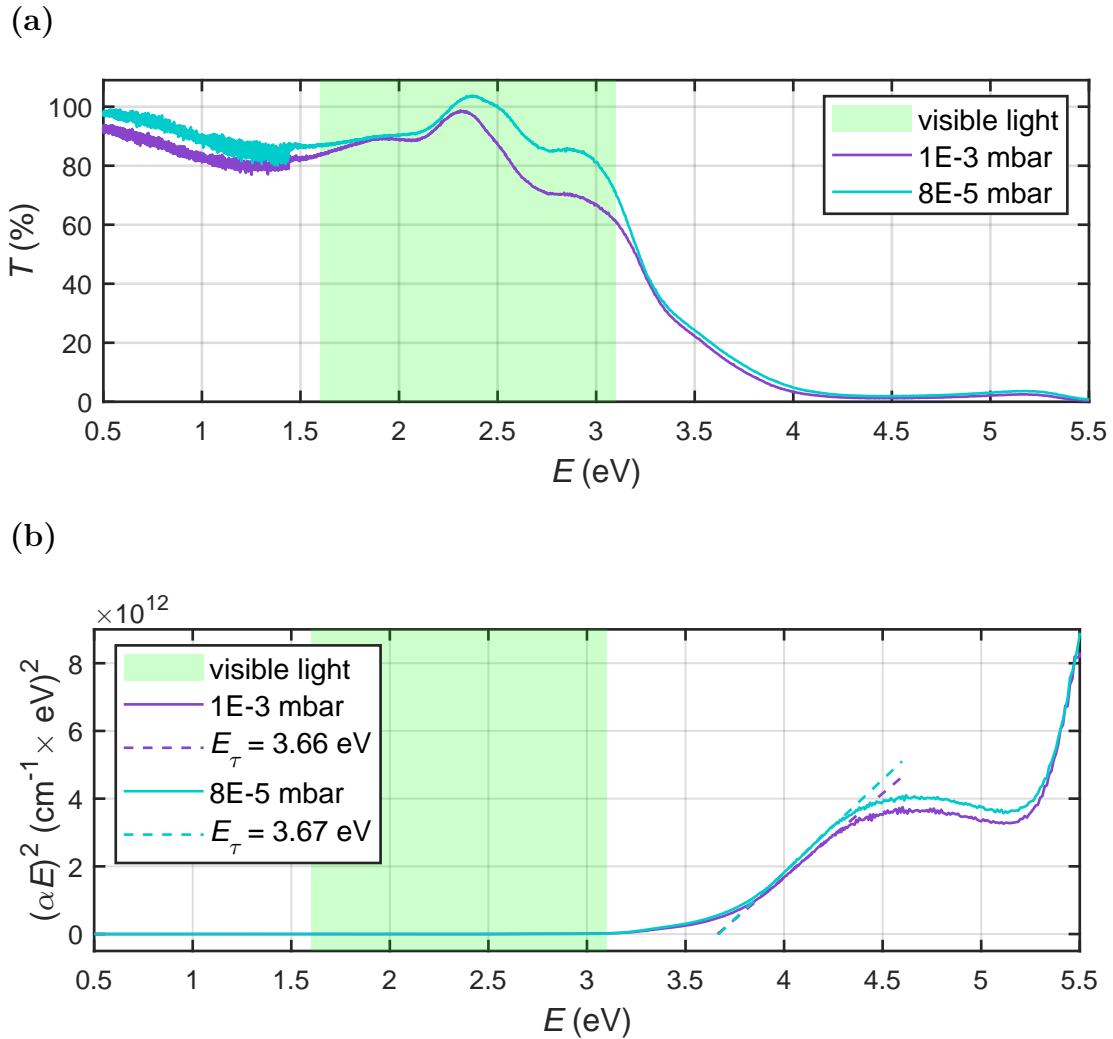


Figure 3.5: (a) Transmission spectra of two selected Cr_2O_3 thin films, deposited with different oxygen partial pressures. The spectra are normalized to a corresponding uncoated m -plane sapphire substrate. (b) Tauc-plot of the above-mentioned samples. It is assumed that Cr_2O_3 has a direct bandgap [13, 25].

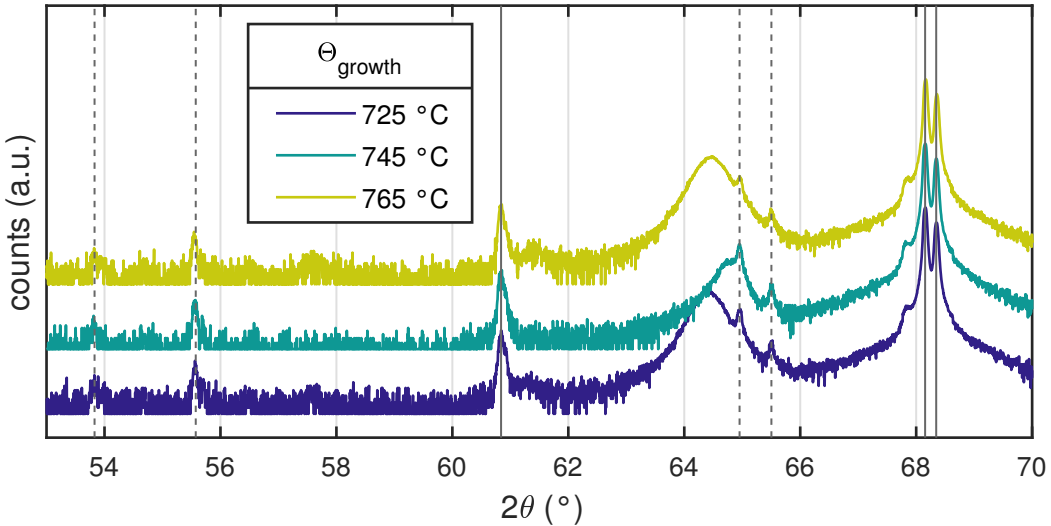


Figure 3.6: 2θ - ω -pattern of Cr_2O_3 thin films deposited on *m*-plane sapphire for three different growth temperatures. The lines indicate substrate reflections that stem from copper and tungsten radiation (cf. 3.1)

practice to clean the latter every couple of processes due to coating with target material which absorbs laser energy. But from Fig. 3.7b it becomes clear that this should be done much more frequently when working with Cr_2O_3 . Note that the laser has a wavelength of 248 nm, corresponding to 5.0 eV, which is not transmitted by Cr_2O_3 thin films⁽⁵⁾, as can be seen in Fig. 3.5a. Therefore, the increasing coating of the laser entrance window with each new process absorbs a large amount of laser pulse energy, resulting in less fluence on the PLD target. This results in less ablated target material and less kinetic energy of the ablated species, which leads to a reduced growth rate and different crystal growth conditions that have higher strain and ω -FWHM as a result.

This explanation is supported by the dependence of crystal quality on oxygen partial pressure (cf. Fig. 3.2). There, the increment of crystal quality with higher oxygen pressures is attributed to the increased background gas scattering resulting in less kinetic energy of the plasma material. This also explains the outlier in Fig. 3.7a, where one sample corresponds to a higher strain and ω -FWHM of approx. 0.9 % and 41', respectively (black square). This is not expected when considering the rather small growth rate of 3 pm pulse^{-1} (W6724 in Fig. 3.7b). But when taking account for the fact that this sample is fabricated at a very low oxygen partial pressure of 8×10^{-5} mbar, it becomes clear that although the reduced fluence on the target would generally lower the kinetic energy of the plasma material, the limited scattering with the background gas counteracts this effect, resulting in the observed crystal quality.

It is noteworthy that the observed strain (cf. Fig. 3.2a) is distributed around two distinct values of approx. 0.4 % and 0.9 %. A prior reported thin film tilt for *m*-plane oriented rhombohedral heterostructures [46] may be the reason for this observation: the samples are installed in the XRD device in such a way that the *c*-axis is either parallel or orthogonal to the scattering plane. This orientation is arbitrary, and thus

⁽⁵⁾ To be precise, the transmission spectrum in Fig. 3.5a is recorded for *m*-plane oriented *crystalline* Cr_2O_3 thin films. This may not be the present phase when Cr_2O_3 deposits on the (colder) window made out of glass, where it may form an amorphous phase.

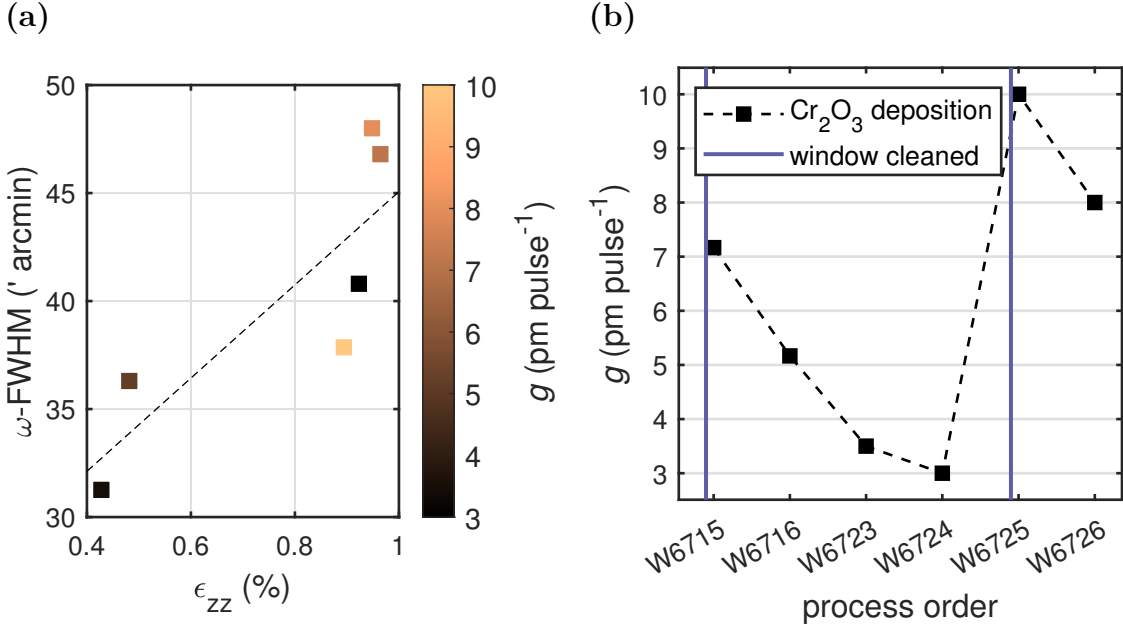


Figure 3.7: (a) Correlation of ω -FWHM with o.o.p. strain, as well as correlation of both with growth rate g (false color). The dashed line is a linear fit serving as guide to the eye. (b)

the (expected) thin film tilt is either along the X-ray beam or perpendicular to it, which could result in unexpected results when calculating the o.o.p. lattice plane distance from the observed peak position. To check if this is the origin of the observed strain, for two samples of different strain according to Fig. 3.2, four 2θ - ω -scans were performed with incrementing the azimuth by 90° after each measurement. The resulting diffraction patterns are depicted in Fig. 3.8. The strain is independent of azimuth, only the peak intensity is altered by the in-plane rotation of the sample. For both samples, an azimuth of 0° and 180° results in a lower intensity, supporting the hypothesis that the (expected) thin film tilt is perpendicular to scattering plane which results in a deviation from the BRAGG condition. Therefore, the distribution of observed strain is not a measurement artifact.

Deposition on *c*-, *r*-, *m*- and *a*-plane Sapphire

For the samples deposited on substrates with different orientation, 2θ - ω -patterns were recorded (Fig. 3.9). For each sample, the expected substrate peaks are observed: (00.6) and (00.12) for *c*-plane; (01.2), (02.4), (03.6) and (04.8) for *r*-plane; (30.0) for *m*-plane; (11.0) and (22.0) for *a*-plane. Several smaller peaks also correspond to those reflections but stem from other X-rays than Cu-K α (cf. Fig. 3.1). The mentioned reflections are also observed for the Cr₂O₃ thin film, but with a shift in 2θ position similar to the previously investigated *m*-plane samples (Tab. 3.1). Note that for *r*-plane, the higher order reflections of Cr₂O₃ cannot be observed. It can be concluded that Cr₂O₃ grows in the α -phase on sapphire substrates of different orientation, where the thin film orientation matches the corresponding substrate. Henceforth, “*c*-plane Cr₂O₃” will refer to a Cr₂O₃ thin film deposited on *c*-plane oriented 5×5 mm 2 sapphire substrates, and so on. For each sample, ω -scans were performed on the (00.6), (02.4), (30.0) and (11.0)

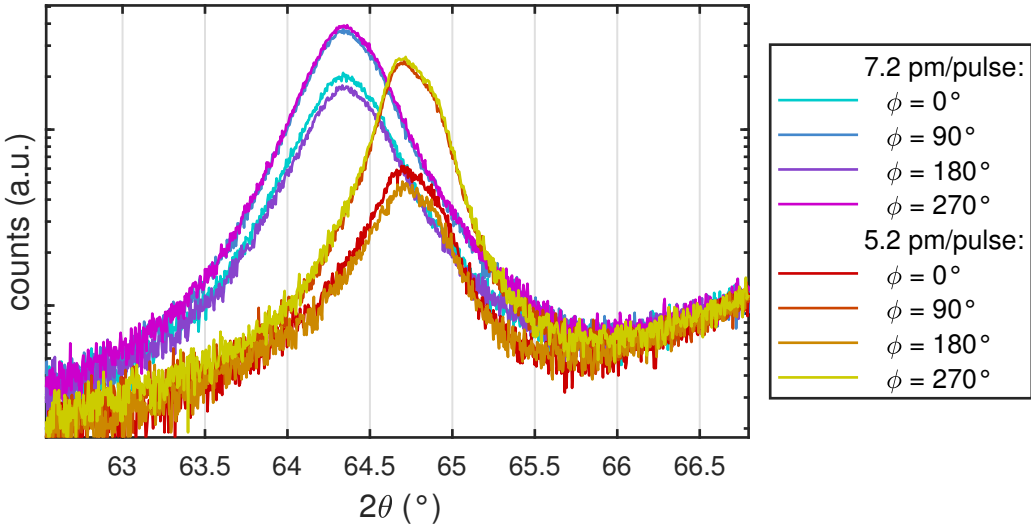


Figure 3.8: 2θ - ω -patterns for two samples in four different azimuths each.

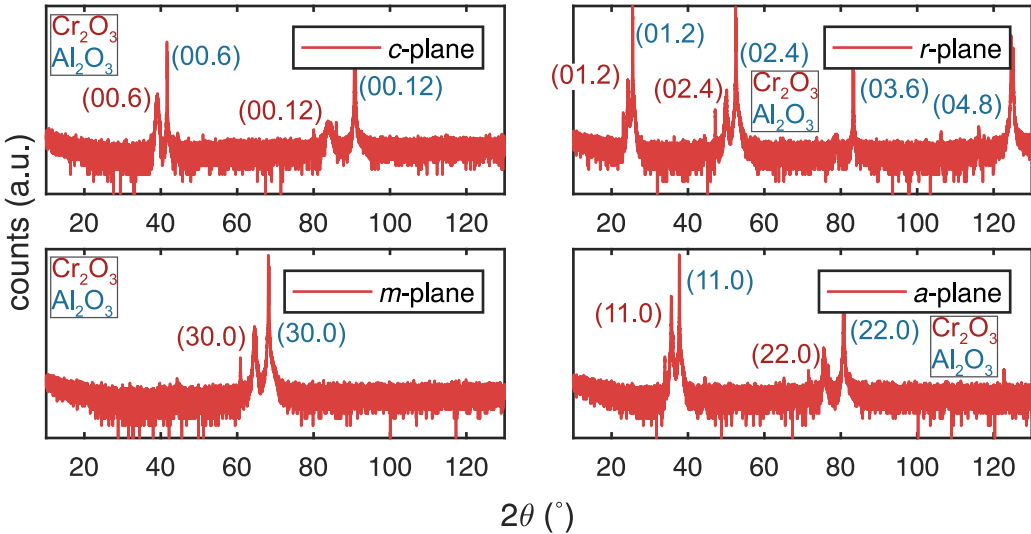


Figure 3.9: 2θ - ω -patterns of Cr_2O_3 thin films deposited on c -, r -, m - and a -plane sapphire.

Table 3.1: Structural parameters, approximate resistivity at room temperature and activation energy for Cr_2O_3 thin films of different orientation.

Plane	ϵ_{zz} (%)	ω -FWHM (')	ρ (Ωcm)	E_A (meV)
c	1.71	42.6	3	57, 34
r	0.72	38.4	120	117
m	0.55	42.6	3600	240
a	1.41	32.4	4900	259

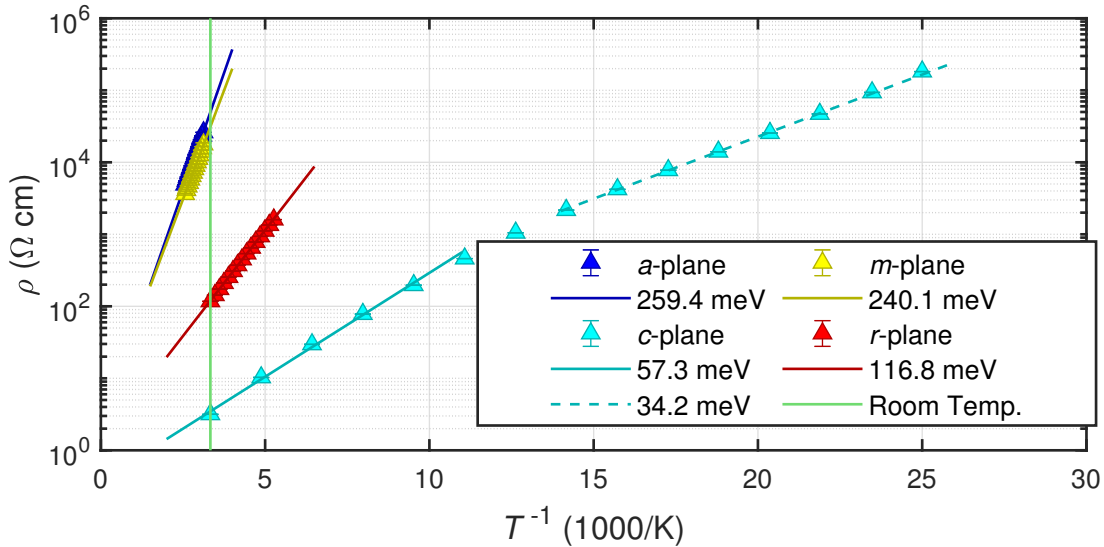


Figure 3.10: Temperature dependent resistivity measurements for samples with different orientations.

reflections for *c*-, *r*-, *m*- and *a*-plane, respectively. The resulting ω -FWHMs are in the range of approx. $30'$ to $40'$ (Tab. 3.1).

Because the resistivity of all samples was too high to measure Hall effect, only resistivity measurements (cf. 2.3.2) were performed for several temperatures (Fig. 3.10). The resistivity depends strongly on the orientation of the thin film, the resistivities at room temperature are listed in Tab. 3.1. A difference of more than three orders of magnitude between *c*-plane and *a*-plane samples is observed. The linear behavior of the ARRHENIUS-plot⁽⁶⁾ indicates a thermally activated mechanism for conductivity, and thus semiconductive behavior. Note that no further conclusions can be drawn on the conduction mechanisms due to the missing carrier concentration and mobility data. By assuming a behavior of the form

$$\rho \propto \exp\left(\frac{E_A}{k_B T}\right), \quad (3.2)$$

with BOLTZMANN constant k_B , an activation energy E_A can be estimated. Those energies are also listed in Tab. 3.1. For *c*-plane Cr_2O_3 , two linear regimes can be distinguished, favoring a dependence of the form

$$\rho \propto a \exp\left(\frac{E_{A,1}}{k_B T}\right) + b \exp\left(\frac{E_{A,2}}{k_B T}\right), \quad (3.3)$$

thus two activation energies are determined.

3.1.3 Conclusion

m-plane Cr_2O_3 thin films can be deposited over a wide range of oxygen partial pressure of more than 2 orders of magnitude. It turned out that the main influence on the crystal quality correlates with the growth rate and is due to a variation of the laser pulse fluence

⁽⁶⁾ Visualization of $f(T)$ as $f'(\tau)$ with $f' = \log f$ and $\tau = 1/T$.

on the target. Nevertheless, an oxygen partial pressure of 1×10^{-3} mbar and a growth temperature of 750 °C are chosen for deposition of subsequent thin films. $\alpha\text{-Cr}_2\text{O}_3$ could also be deposited on *c*-, *r*- and *a*-plane sapphire, with the thin films crystallizing in the respective orientation. Note that all deposited thin films showed a discrepancy between observed o.o.p. lattice plane distance and values predicted from Tab. 1.1. The conductivity is strongly dependent on the crystal orientation and was very low for the prismatic orientations, but with 0.3 S cm^{-1} three orders of magnitude higher for the basal orientation.

3.2 Doping of Cr₂O₃ Thin Films

The resistivity of the Cr₂O₃ thin films showed strong dependence on thin film orientation. To improve and tailor the conductivity, it is tried to incorporate acceptors into the *p*-type material. The elements chosen for this are Cu and Zn, because doping has already been accomplished on *c*-plane sapphire with magnesium via MgO [25]. Furthermore, it is tried to reduce the sheet resistance of the contacts of the thin films.

3.2.1 Experiment

To fabricate doped thin films, three different PLD targets were applied. Each target was elliptically segmented (cf. 2.1.1), with the outer region consisting of pure Cr₂O₃. The inner region (ellipse) was also Cr₂O₃ but with a fraction of dopant, namely:

1. 0.01 wt.% CuO, called “CuO-doped”,
2. 0.01 wt.% ZnO, called “ZnO-doped (low)” and
3. 1 wt.% ZnO, called “ZnO-doped (high)”.

For each target, several processes were done with the laser spot position varying on the target. For each process, deposition was done on all of the 4 aforementioned substrate orientations to check whether the conductivity of the prismatic orientations could be improved. The composition of the ablated material can be calculated via Equ. 2.1, but this does not account for the finite area illuminated by the laser pulse. A simple model for including this effect can be achieved by simulating N several randomly distributed points r_i in the range Δr around a radial laser position r_{PLD} . Then, the composition x_D can be calculated as the mean of the N calculated compositions for each r_i . The resulting dependence of x_D on r_{PLD} is visualized in Fig. 3.11a, where a higher value of Δr results in more smeared out graphs. A target with inner concentration of 0.01 wt.% dopant was assumed (Cu-doped target or Zn-doped (low) target). The Monte Carlo simulations can further be approximated by a linear fit, which was done for $\Delta r = 2$ mm (blue dotted line in Fig. 3.11a). Henceforth, the different samples fabricated with different radial laser spot positions r_{PLD} are characterized by the expected composition x_D calculated from this linear fit. The reason for this is that according to Equ. 2.1, when applying r_{PLD} smaller than the length of the semi-minor axis of the inner ellipse, no variation in composition would be observed, even though the real finite laser spot size results in a different result. Note further that due to the small concentration of dopant, it is not possible to resolve those fractions via element sensitive measurements. Dr. Daniel Splith kindly performed Energy-dispersive X-Ray Spectroscopy (EDX) measurements that resulted in no signal for either Cu or Zn that was above the noise level.

To improve the contacts for resistivity measurements, samples were produced using the ZnO-doped (low) target and a fixed $r_{PLD} = 3$ mm. Only *c*- and *r*-plane sapphire substrates were used and the deposition temperature was varied between 560 °C and 680 °C. For each growth temperature, subsequent contacting was done with Ti-Al-Au for a *c*-plane and an *r*-plane sample, as well as Ti-Au for a *c*-plane and an *r*-plane sample. Furthermore, the *c*-plane samples contacted with Ti-Al-Au were compared before and after annealing at 210 °C in nitrogen atmosphere.

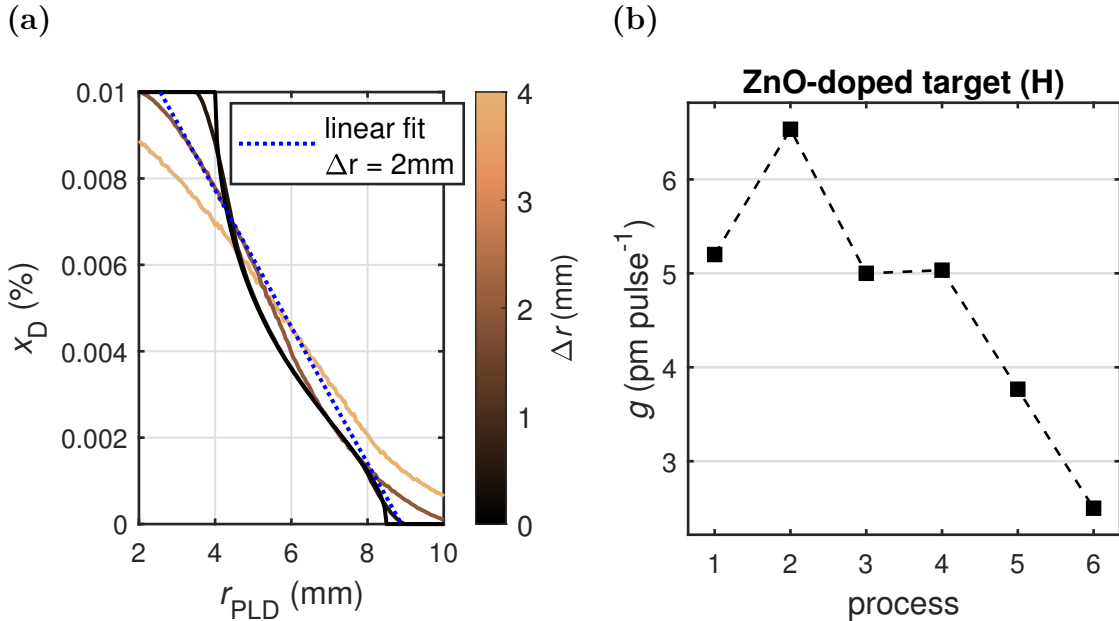


Figure 3.11: (a) Predictions for the plasma plume composition x_D using Monte Carlo simulations with $N = 10\,000$ and different values for Δr . The blue dotted line is a fit for the Graph calculated with $r = 2 \text{ mm}$. (b) Growth rate depending on the process order for the samples fabricated from the ZnO-doped (high) target. The laser entrance window was cleaned after each process.

2θ - ω -scans were performed for every sample, but ω -scans for c - and r -plane samples only. The thickness was determined using spectroscopic ellipsometry. Resistivity measurements at room temperature were done using the PAUW method, which was also applied when conducting temperature dependent resistivity measurements on one c -plane sample of each target. Note that the effect of infrequent cleaning of the laser entrance window that was described in 3.1 was discovered during the execution of those experiments, which is why the samples produced from the ZnO-doped (high) target were the only ones for which this effect could be prevented. Furthermore, 40 000 pulses were applied for the samples fabricated from the CuO-doped and ZnO-doped (low) target, as well as one sample from the batch made with the ZnO-doped (high) target. All other samples from this batch were deposited with 30 000 pulses.

3.2.2 Results

Laser Position Variation for Different Targets

The growth rates of the samples produced from the CuO-doped and ZnO-doped (low) target are depicted in Fig. 3.12. The growth rates vary between 3 and 6 pm pulse $^{-1}$ and depend strongly on the number of deposition processes that were conducted before. After cleaning the laser entrance window, and thus reducing laser energy absorption, the growth rate can be increased. This is similar to the results obtained in 3.1.

However, the growth rates depending on the fabrication order for the ZnO-doped (high) samples are depicted in Fig. 3.11b. Note that the growth rate varies from approx. 2.5 to 6.5 pm pulse $^{-1}$, even though the laser entrance window was cleaned after each

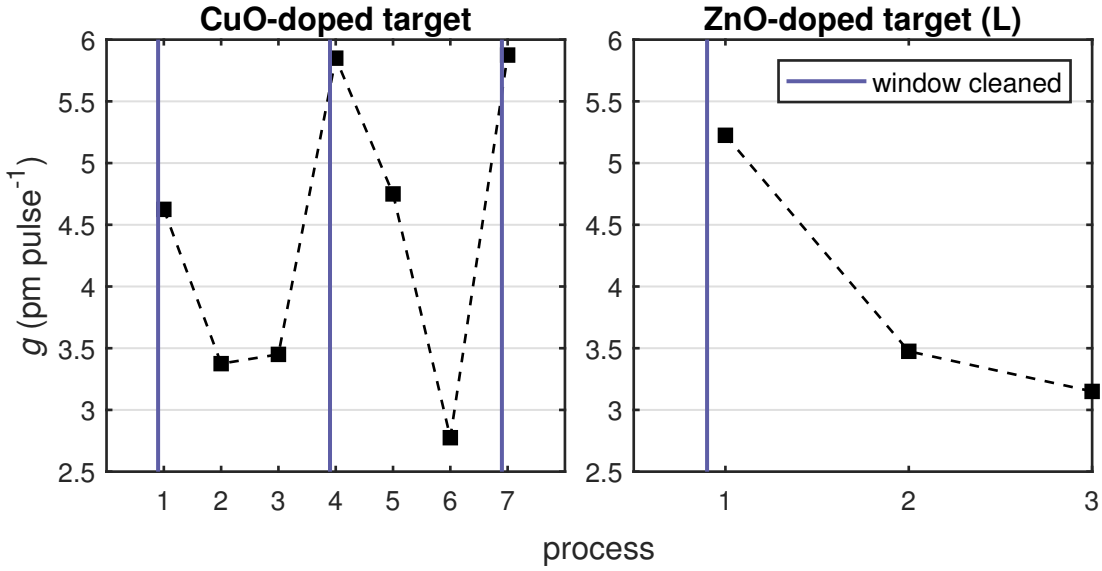


Figure 3.12: Growth rate depending on the process order for the samples fabricated from the CuO-doped and ZnO-doped (low) target. It is indicated when the laser entrance window was cleaned.

process. So this variation in growth rate must be traced back to another effect. Only the first sample was fabricated with 40 000 pulses, which explains the increment of growth rate between the first and second process: Due to the higher number of pulses, the laser entrance window gets more coated and thus the last 10 000 pulses reduce the average growth rate. Furthermore, the second process was done with $r_{PLD} = 6\text{ mm}$, which is rather outside compared to the 1st, 3rd and 4th process with 3 mm, 4 mm and 2 mm, respectively. This results in a larger total ablated area and in less target degradation. Therefore, the hypothesis is that target degradation during deposition has an influence on the growth rate. This is supported by the observation of incremental reduction of growth rate for processes 1, 5 and 6. Note that all these samples were fabricated with $r_{PLD} = 3\text{ mm}$ and otherwise the same deposition parameters. The only variation is that tracks are carved into the target by the laser (Fig. 3.13c). This is probably the reason for a crucial change in plasma dynamics and therefore a reduction of the growth rate from approx. 5 to 2.5 pm pulse $^{-1}$.

For the samples with high conductivity, namely c -plane and r -plane, ω -scans were performed on the (00.6) and (02.4) reflection, respectively. The extracted ω -FWHMs are depicted in Fig. 3.14 depending on the growth rate for the respective process. A general trend is that the crystallinity increases for lower growth rates. It is not relevant, whether this reduction in growth rate is due to less fluence on the laser target due to infrequent window cleaning (CuO-doped and ZnO-doped (low) target) or due to target degradation (ZnO-doped (high) target). The better FWHM is achieved for c -plane samples. Note that for the deposition of Cr₂O₃ on r -plane sapphire from the ZnO-doped (high) target, no thin film peaks in 2θ - ω -scans (see below) were observed. Those X-ray-amorphous films are presumably a result of the drastically altered plasma dynamics due to target degradation.

In Fig. 3.15a, the measured resistivity at room temperature depending on the predicted dopant concentration is depicted. From the unsystematic variation in resistivity

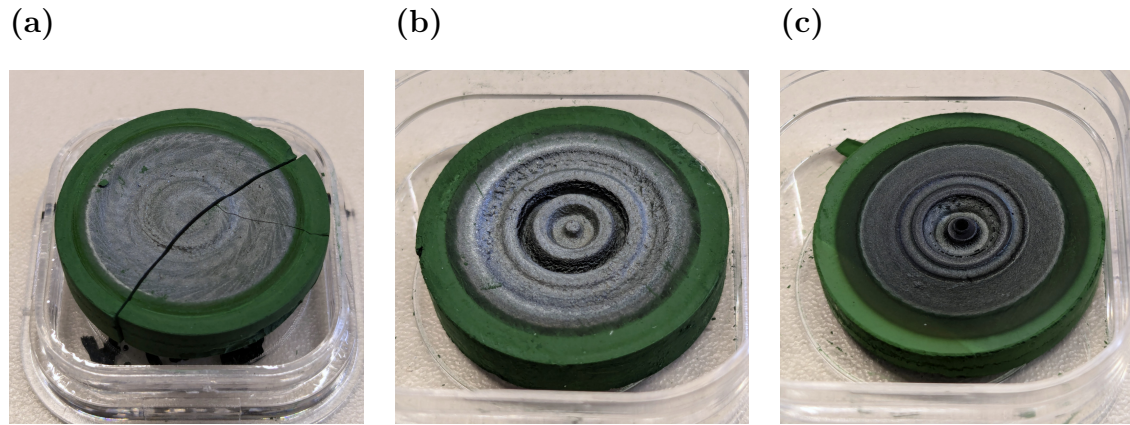


Figure 3.13: Photograph of the (a) CuO-doped, (b) ZnO-doped (low) and (c) ZnO-doped (high) target. The CuO-doped target broke during the last process where it was used. The silverish tint is presumably due to formation of metallic chromium oxide on the target surface.

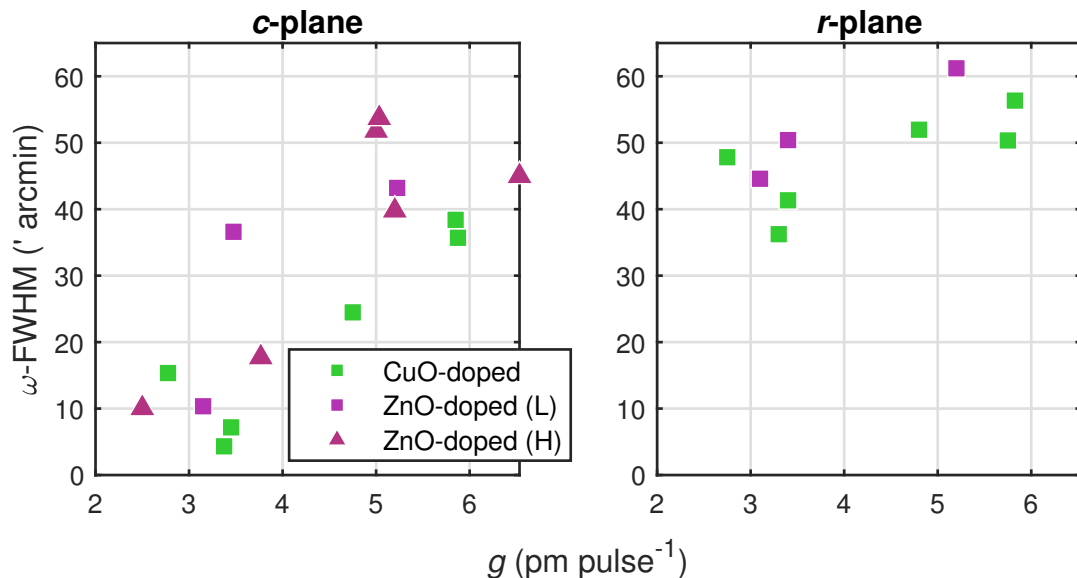


Figure 3.14: ω -FWHM for *c*- and *r*-plane samples that were fabricated from the three radially segmented targets.

Table 3.2: Activation energies E_A extracted from the linear regimes in the temperature dependent resistivity measurements (Fig. 3.16).

target	E_A (meV)	
	< 100 K	> 100 K
CuO-doped	53	83
ZnO-doped (low)	35	61
ZnO-doped (high)	31	50
pure Cr_2O_3	35	54

(2 to $500 \Omega \text{cm}$), it can be concluded that the attempt of doping the Cr_2O_3 thin films resulted in no improvement of conductivity. Using the two targets with different concentration of ZnO in the inner ellipse, no change was observed when adjusting x_D between 0.001 % and 1 %. Note the aforementioned samples that were all fabricated with $r_{\text{PLD}} = 3 \text{ mm}$ on the ZnO-doped (high) target, corresponding to the triangles in Fig. 3.15a at approx. $x_D = 1 \%$: here, the same process parameters yield samples differing in resistivity by 2 orders of magnitude. Because those samples showed different growth rates due to target degradation, it is plausible that this also influences the conductivity.

The growth rate influences the crystal quality (cf. Fig. 3.14) and therefore, in Fig. 3.15b, the resistivity depending on the ω -FWHM is depicted. It becomes clear that a higher mosaicity results in higher conductivity. Since more dislocations correspond to more crystal defects (cf. 1.3.2), this result is in accordance to the predicted influence of crystal defects on the electrical properties of Cr_2O_3 thin films (cf. 1.2.1). It has to be noted that this effect is less pronounced for r -plane samples compared to c -plane samples. Furthermore, this does not explain why m - and a -plane Cr_2O_3 exhibit such higher resistivity, because their ω -FWHM is comparable to the basal and pyramidal orientations (cf. Tab. 3.1).

For each target, one c -plane sample with presumably highest doping concentration (smallest r_{PLD}) was chosen to perform temperature dependent resistivity measurements in the range of 40 to 390 K (Fig. 3.16). For all samples, an ARRHENIUS-like behavior is observed with two linear regimes above and below 100 K, respectively. By applying Equ. 3.3, two activation energies can be extracted that are listed in Tab. 3.2.⁽⁷⁾ Note that the (arbitrary) choice, which samples were measured for each target, determined the absolute difference in resistivity: There are in fact samples fabricated from the CuO-doped target that have lower resistivity than samples fabricated from the ZnO-doped targets (cf. Fig. 3.15).

Even though the doping resulted in no improvement of the electrical properties of the thin films, the several samples fabricated at different growth conditions⁽⁸⁾ may serve as an insight into the o.o.p. strain that was already observed in 3.1. To check whether the hypothesis of increasing strain with increasing growth rate is also true for orientations other than m -plane, the o.o.p. strain dependent on the growth rate is depicted in

⁽⁷⁾ **Soll ich dazu noch mehr sagen? Ich weiß nicht, ob man sehr viel aus diesen Zahlen lernen kann.**

⁽⁸⁾ Even though these differences were achieved accidentally: by infrequent laser entrance window cleaning and repeated ablation on targets with the same laser spot position r_{PLD} .

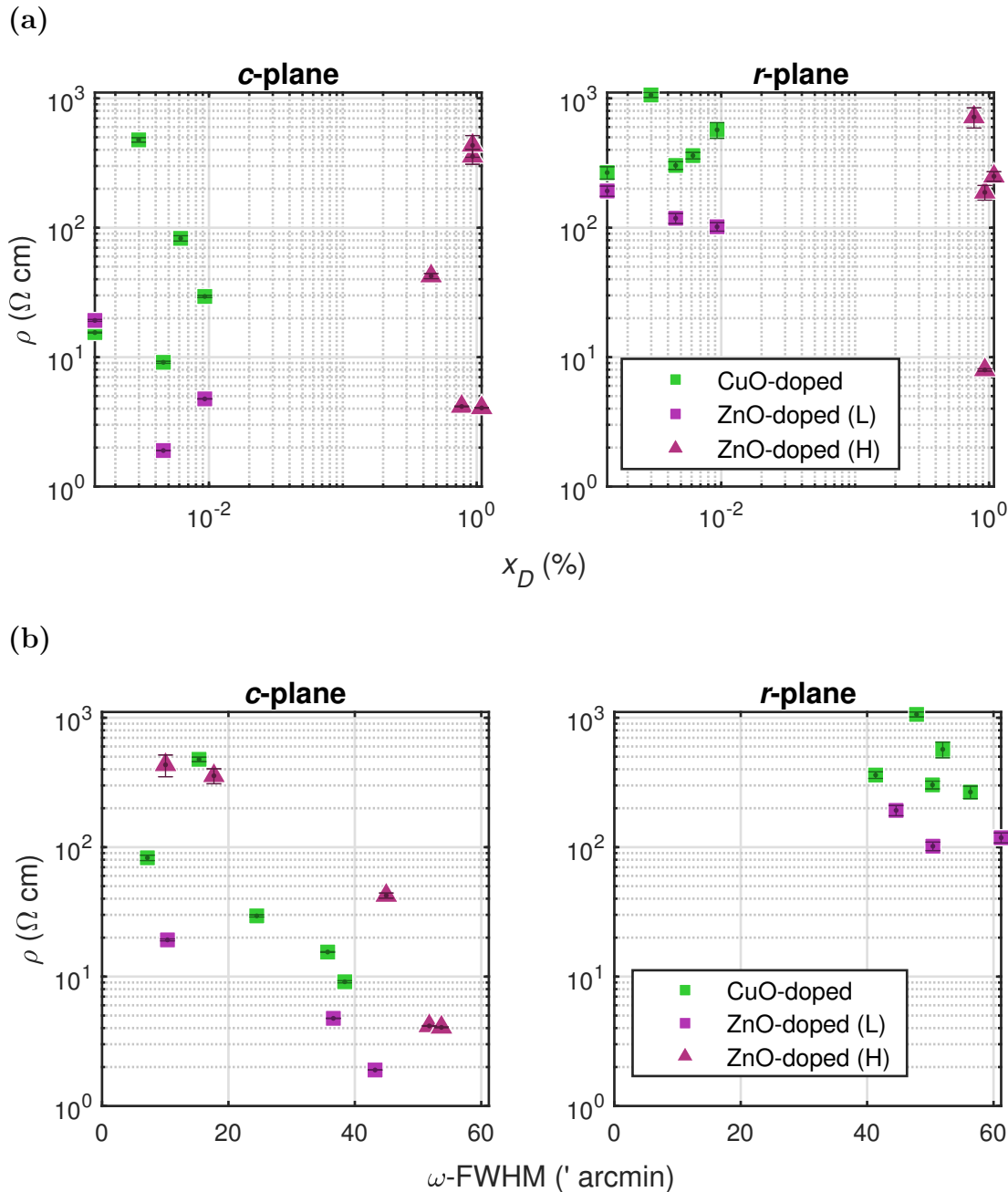


Figure 3.15: (a) Resistivity vs. predicted dopant concentration for *c*- and *r*-plane samples fabricated from all three radially segmented targets. (b) Resistivity vs. ω -FWHM (' arcmin) of the aforementioned samples.

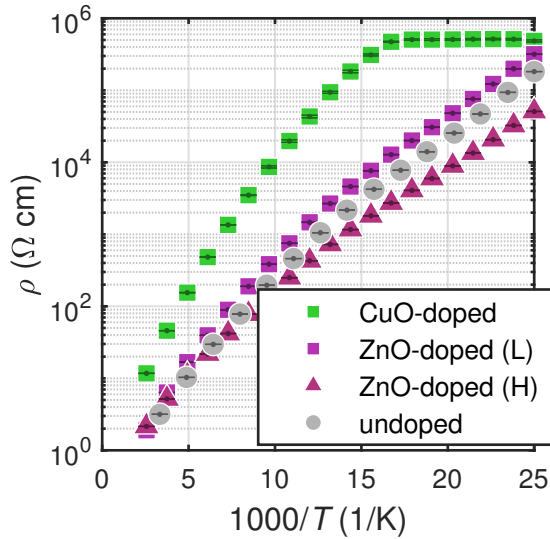


Figure 3.16: Temperature dependent resistivity measurements for *c*-plane samples fabricated from the different radially segmented targets, as well as a pure Cr_2O_3 target. The clipping of the sample from the CuO-doped target (green squares) is due to the limited resolution of the measurement device and the artifact nature of this saturation is confirmed by repeated measurements with different current applied during measurement (not shown).

Fig. 3.17a. For *m*- and *a*-plane, this behavior can indeed be observed. However, the slope of this relation differs depending on the target: the samples fabricated from the CuO-doped target showed less strain depending on growth rate than the samples fabricated from the ZnO-doped (high) target. This may be explained by the fact that the target degradation for the former (cf. Fig. 3.13a) was not so pronounced when compared to the latter (cf. Fig. 3.13c).

A reverse behavior is observed for *c*-plane samples: the strain is increasing with higher growth rates. But compared to *m*- and *a*-plane, there is no significant difference between the samples fabricated from different targets. This leads to the assumption that the plasma dynamics do not determine the o.o.p. strain for this orientation. It has to be noted that due to the constant pulse number, a change in growth rate corresponds to a change in thickness of the thin films. Therefore, it may be possible that the strain of the thin samples (low growth rate) is due to pseudomorphic growth on the corresponding Al_2O_3 substrate. Note that this leads not to the conclusion that the origin of the strain in *m*- and *a*-plane samples is also pseudomorphic growth: There, the thicker samples show more strain which is not expected because far away from the interface, dislocations should form to propagate relaxed growth. For *r*-plane samples, the overall strain is smaller and shows a less pronounced trend similar to *m*- and *a*-orientation. Because *r*-plane has both basal and prismatic character, both thickness and plasma dynamics effects may contribute to the observed strain.

The qualitative difference between *c*-plane and the other orientations can also be observed in Fig. 3.17b, where the ω -FWHM is shown depending on the o.o.p. strain. Compared to the previous results (cf. Fig. 3.7a), both factors characterizing crystal quality (strain and ω -FWHM) are not minimized simultaneously.

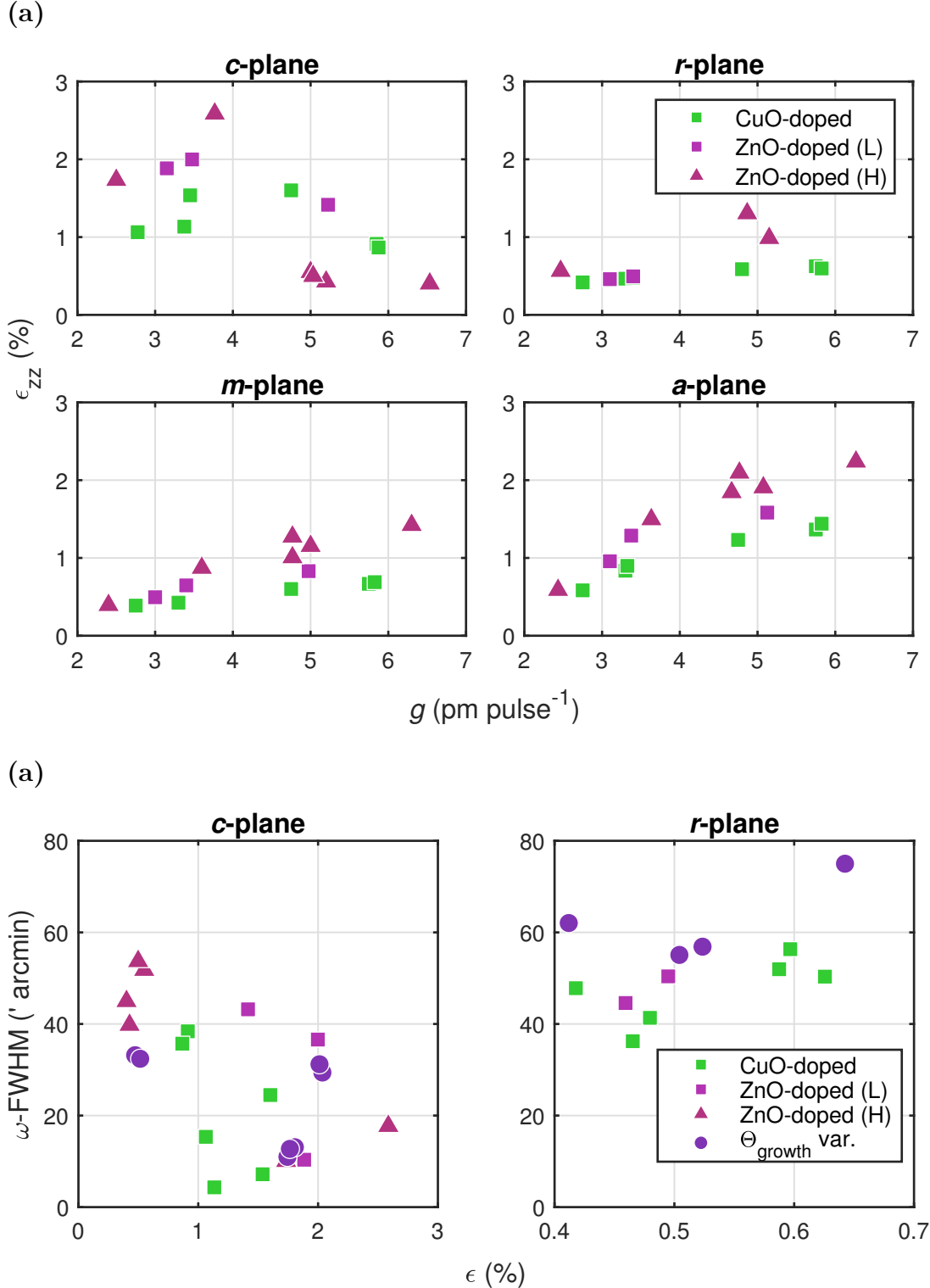


Figure 3.17: (a) Strain extracted from the peak positions in $2\theta\text{-}\omega$ -scans for samples fabricated from the three radially segmented targets. (b) Correlation between strain and $\omega\text{-FWHM}$ for *c*- and *r*-plane samples. The samples fabricated at different growth temperatures are also included.

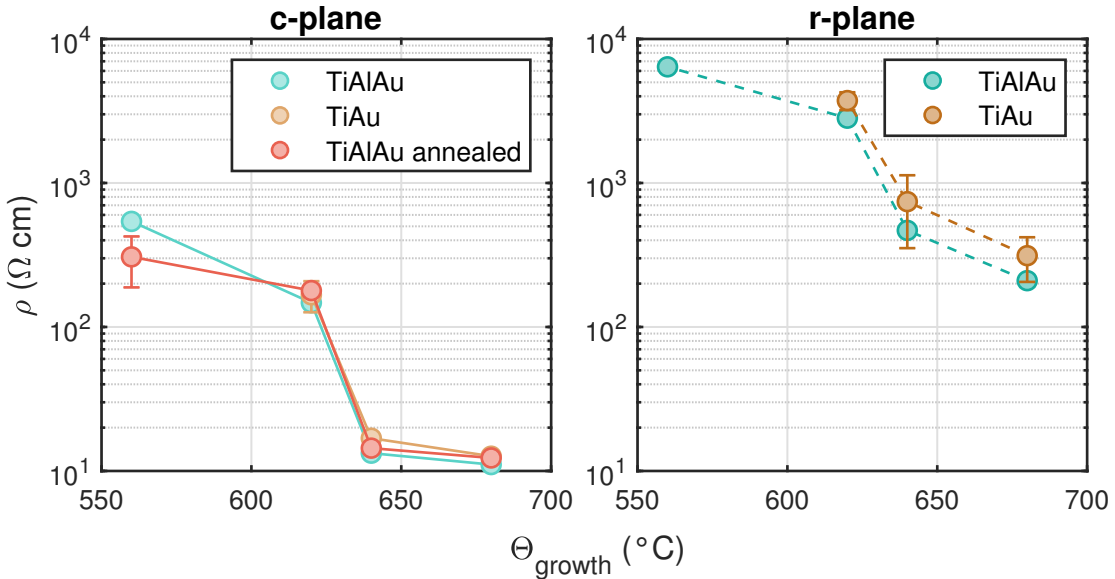


Figure 3.18: Resistivity measured at room temperature depending on growth temperature. Three different contact types were applied.

Ohmic Contact Optimization

For both *r*- and *c*-plane, a reduction in growth temperature results in higher crystallinity (not shown). Lower growth temperatures also yield higher resistivities, as shown in Fig. 3.18. This confirms the previously observed result, that the crystallinity reduces conductivity. It has to be noted that several effects influence the change in ω -FWHM: The first process was done at highest temperature, which was then gradually reduced. So the temperature reduction is convoluted with a process order effect. This is important, because for every sample, the same radial laser spot position $r_{\text{PLD}} = 3 \text{ mm}$ was used on the ZnO-doped (low) target, which led to increasing surface degradation (cf. Fig. 3.13b). This results, as shown before, in lower growth rates and higher crystallinities. This effect is supported by the fact that the window was cleaned before the first process only, which also adds to the subsequent reduction of laser fluence on the target surface. Therefore, the effect of temperature variation is covered by those growth rate effects, which makes it difficult to deconvolute the influence of growth temperature on conductivity. As can also be seen in Fig. 3.18, no significant change in resistivity was observed for both the variation between Ti-Al-Au and Ti-Au contacts, as well as between annealed and as-deposited contacts. For *r*-plane, the Ti-Al-Au contacts yielded slightly better conductivities.

3.2.3 Conclusion

The incorporation of CuO or ZnO had no effect on the conductivity of *c*- and *r*-plane oriented Cr_2O_3 thin films. None of the *m*- or *a*-plane oriented films became conductive. However, the conductivity depends strongly on the crystallinity, which indicates intrinsic defects as the origin of charge carriers. The crystallinity is mainly influenced by target degradation due to repeated ablation with the same laser spot position on the target. This results in lower growth rates and presumably less kinetic energy of

the plasma species which deposits on the substrate. Even though the doping attempt showed no effect, a discrete material library of Cr_2O_3 thin films with different strains was provided. A fundamental difference between *c*-plane and the other common orientations was observed, regarding the origin of the observed o.o.p. strain. Further measurements must be conducted to deconvolute the effects of (i) thickness, (ii) laser fluence on target and (iii) target degradation.

3.3 Strain Analysis

The structural properties of the thin film, namely its mosaicity and lattice distortion depend crucially on the growth process. It turned out that the absorption of energy at the laser entrance window alters the growth rate and the crystallinity much more dominantly than the growth temperature or the oxygen partial pressure (cf. 3.1). A similar effect was observed when targets were used for fabrication that exhibit a non-planar surface and tracks that were carved during previous ablations (cf. 3.2). Because the structural properties of the thin film also influence its electrical properties (cf. 3.2), the following investigations focus on the origin of the observed variations in strain and ω -FWHM. This is further motivated by the observation that a deliberate and controlled variation of laser spot size on the target surface yields a large reduction of ω -FWHM as well as a reduced shift of the peak position in the 2θ - ω -pattern (Fig. 3.19). This was achieved by varying the lens position (cf. 2.1) such that the laser spot size increases, yielding smaller fluence and larger ablation area on the target surface.

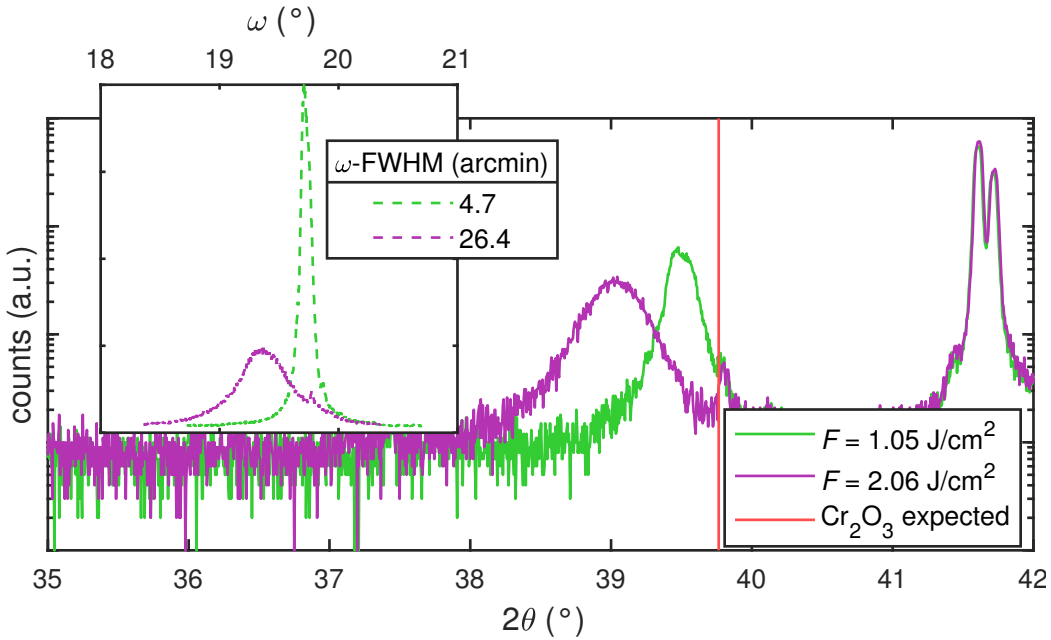


Figure 3.19: 2θ - ω -patterns for two *c*-plane samples fabricated with different laser focus on the target. The inset displays the diffractograms of the corresponding ω -scans performed on the respective reflections. The ZnO-doped (low) target was used without a fixed *rPLD* but with uniform ablation on the whole target surface.

3.3.1 Experiment

Sample Fabrication

For all following depositions, the laser entrance window was cleaned before each process. A pure Cr_2O_3 target was used for deposition of thin films on $5 \times 5 \text{ mm}^2$ sapphire substrates in the four aforementioned orientations. The first batch of samples was produced by only varying the pulse number to achieve a series of thin films with varying

thickness but constant laser fluence during deposition⁽⁹⁾. The pulse energy was set to 650 mJ and the lens position⁽¹⁰⁾ to -2 cm , the resulting fluence is approx. 2 J cm^{-2} . This corresponds to the standard configuration during all previous processes (pink square in Fig. 2.2). This was repeated with fewer pulse number variations for three other lens positions, namely 0 cm , 1 cm and 2 cm , resulting in lower fluences: In Fig. 2.2, the yellow circles represent the probed laser fluences. This set of samples is referred to as the 1st batch.

To investigate the influence of fluence independent of ablation area, a 2nd batch of samples was fabricated with a fixed lens position (-1 cm) but varying laser pulse energy: 300 mJ, 450 mJ, 650 mJ and 800 mJ. The pulse number was adjusted to achieve approximately same thicknesses. The achieved fluences are visualized as red triangles in Fig. 2.2.

Measurements

For all samples, $2\theta\text{-}\omega$ -scans as well as ω -scans were performed. The reflections probed by the latter were (00.6) , (02.4) , (30.0) and (22.0) for c -, r -, m - and a -plane, respectively. For some selected samples of different thickness and fluence from the 1st batch, transmission measurements have been performed. The thickness of all samples was determined by spectroscopic ellipsometry measurements. To obtain more information about the relation between in-plane and out-of-plane lattice constants, RSMs were performed on selected samples:

c-plane For c -plane samples, the thickness series of the 1st batch that was fabricated with the largest laser spot size (lowest fluence) was investigated. The asymmetric reflection that was used for probing the relaxation process is (02.10) , which has an inclination angle of approx. 32° with respect to the sample surface.

r-plane All r -plane samples fabricated in the 2nd batch with different laser pulse energies were investigated. For each sample, the x -axis of the sample – containing the projection of the c -axis – is found by performing a φ -scan on the (03.0) reflection: This set of lattice planes has an inclination with respect to the surface, so the position of the peak in the diffraction pattern of the φ -scan reveals the x -axis. In this azimuth, an RSM is recorded around the asymmetric (03.0) reflection and the symmetric (02.4) reflection. By rotating $\Delta\phi = 90^\circ$, the y -axis lays in the scattering plane and another RSM is performed around the symmetric (02.4) reflection. The twofold measurement of the symmetric reflection is necessary to calculate a possible lattice plane tilt for both x - and y -direction. Note that no shear is calculated due to the asymmetric nature of the (03.0) reflection with respect to the r -orientation⁽¹¹⁾. After performing the various

⁽⁹⁾ The series of thicknesses that was achieved in the prior experiments was correlated to a series of growth rates.

⁽¹⁰⁾ Note that the values for the lens position have an arbitrary offset; a value of 0 cm does not correspond to the position where the target surface is in focus.

⁽¹¹⁾ For m - and a -plane rhombohedral structures, the crystal is symmetric under the transformation $\phi \rightarrow \phi + 180^\circ$, which is not the case for r -plane.

corrections described in 2.2.4, the tilt angles can be calculated for both azimuths by

$$\theta = \arccos \left(\frac{q_{\perp}}{|\mathbf{q}|} \right) \cdot \operatorname{sgn}(q_{\parallel}), \quad (3.4)$$

with q_{\perp} and q_{\parallel} being the o.o.p. and i.p. components of the scattering vector \mathbf{q} , respectively. The i.p. and o.o.p. strains are determined by comparing the observed scattering vector to the expected scattering vector for the (03.0) reflection:

$$\mathbf{q}_{(03.0)} = |\mathbf{q}_{(03.0)}| \cdot \begin{pmatrix} \cos \alpha_{(03.0)|r} \\ \sin \alpha_{(03.0)|r} \end{pmatrix}, \quad (3.5)$$

with $|\mathbf{q}_{(03.0)}|$ calculated from Equ. 2.6 and Equ. 2.7. $\alpha_{(03.0)|r}$ denotes the angle between the (03.0) reflection and the normal of the r -planes; it can be calculated from Equ. 2.8:

$$\alpha_{(03.0)|r} = 90^\circ - (\alpha_{(03.0)|c} - \alpha_{(01.2)|c}) = \alpha_{(01.2)|c} = 57.62^\circ. \quad (3.6)$$

***m*-plane** Similar to above, all *m*-plane samples from the 2nd batch were investigated. The samples were aligned to the x -axis by performing a φ -scan on the asymmetric (30.6) reflection, and an RSM was recorded afterwards. By rotating $\Delta\phi = 180^\circ$ while maintaining 2θ and ω , the scattering condition for (30.6) is probed and an RSM was recorded. The symmetric reflection (30.0) was also measured in this azimuth. The tilt angle and shear angle can be calculated according to Equ. 3.4 and Equ. 2.13, respectively. The lattice constants can be calculated from the components of the scattering vectors:

$$a_{\perp} = \frac{\sqrt{12}}{q_{\perp}^{(30.\pm 6)}}, \quad (3.7)$$

$$a_{\perp} = \frac{\sqrt{12}}{q_{\perp}^{(03.0)}}, \quad (3.8)$$

$$c = \frac{6}{q_{\parallel}^{(30.\pm 6)}}. \quad (3.9)$$

a_{\perp} denotes the a lattice constant in direction of the normal to the sample surface. By rotating $\Delta\phi = 90^\circ$, the y -axis can be probed via asymmetric reflections (42.0) and (22.0), which differ in the azimuth by $\Delta\phi = 180^\circ$. A second symmetric reflection (30.0) is recorded in this azimuth. Similar to the x -axis, the tilt and shear angles, as well as the lattice constants can be calculated:

$$(4\bar{2}.0) : a_{\perp} = \frac{\sqrt{12}}{q_{\perp}^{(4\bar{2}.0)}}, \quad a_{\parallel} = \frac{2}{q_{\parallel}^{(4\bar{2}.0)}}, \quad (3.10)$$

$$(22.0) : a_{\perp} = \frac{\sqrt{12}}{q_{\perp}^{(22.0)}}, \quad a_{\parallel} = \frac{2}{q_{\parallel}^{(22.0)}}, \quad (3.11)$$

$$(30.0) : a_{\perp} = \frac{\sqrt{12}}{q_{\perp}^{(03.0)}}. \quad (3.12)$$

a_{\parallel} denotes the a lattice constant parallel to the y -axis. For detailed calculations of the former equations, see A.1. Note that all 6 measured reflections yield a value for a_{\perp} , and 2 measured reflections each yield 2 values for c and a_{\parallel} , respectively. Therefore, for each lattice constant, the mean value is evaluated and the error is estimated by the standard deviation.

a-plane All *a*-plane samples from the 2nd batch were investigated and the method is similar to the one applied to the *m*-plane samples. The azimuth of the *x*-axis is found by performing a φ -scan on the (22.6) reflection, which also served for an RSM. Rotating by $\Delta\phi = 180^\circ$ yields the (22.6̄) reflection and (22.0) is also measured. Similar to above, the sample is rotated by 90° to align to the *y*-axis and two more asymmetric reflections are recorded: (30.0) and (03.0). A second RSM of (22.0) is also performed. This yields the following lattice constants for the *x*-axis:

$$a_{\perp} = \frac{4}{q_{\perp}^{(22.\pm 6)}}, \quad (3.13)$$

$$a_{\perp} = \frac{4}{q_{\perp}^{(22.0)}}, \quad (3.14)$$

$$c = \frac{6}{q_{\parallel}^{(22.\pm 6)}}, \quad (3.15)$$

and for the *y*-axis:

$$(30.0) : a_{\perp} = \frac{2}{q_{\perp}^{(30.0)}} \cdot \frac{3}{2}, \quad a_{\parallel} = \frac{2}{\sqrt{3}q_{\parallel}^{(30.0)}} \cdot \frac{3}{2}, \quad (3.16)$$

$$(03.0) : a_{\perp} = \frac{2}{q_{\perp}^{(03.0)}} \cdot \frac{3}{2}, \quad a_{\parallel} = \frac{2}{\sqrt{3}q_{\parallel}^{(03.0)}} \cdot \frac{3}{2}, \quad (3.17)$$

$$(22.0) : a_{\perp} = \frac{4}{q_{\perp}^{(22.0)}}. \quad (3.18)$$

For detailed calculations and the origin of the factor $\frac{3}{2}$, see A.2. Again, lattice constants obtained from several reflections, the mean and standard deviation are calculated.

3.3.2 Results

The analysis of the data will not be structured into the 1st and 2nd batch, but into the analysis of (i) *c*-plane, (ii) *r*-plane and (iii) *m*- and *a*-plane samples. In the following, some general remarks on the fabricated samples will be made.

In Fig. 3.20, a detailed view into the growth rates of the samples of the 1st batch is given. First of all, for a fixed fluence (fixed lens position), increasing the pulse number decreases the growth rate. This is expected, because the coating of the laser entrance window increases during the process. By fixing a pulse number, an increase in growth rate is observed for a regime of decreasing fluence from 2 to 1 J cm^{-2} (Fig 3.20 bottom). This can be explained by the fact that the reduction of fluence is due to increasing laser spot size. When the fluence is still above the ablation threshold for the target material, an increasing ablation area results in an increasing growth rate. But at some point the fluence is too low to ablate the material and then the growth rate decreases, even though the ablation area increases. This can be observed at around 1.2 J cm^{-2} in Fig. 3.20, which is therefore an estimate for the ablation threshold. For the growth rates of the samples of the 2nd batch (Fig. 3.21), a similar conclusion can be drawn. Reducing the laser spot size below approx. 1.5 J cm^{-2} results in a decrease of growthrate from 5 to 2 pm pulse^{-1} . The ablation threshold can be localized between 1 J cm^{-2} and 1.5 J cm^{-2} .

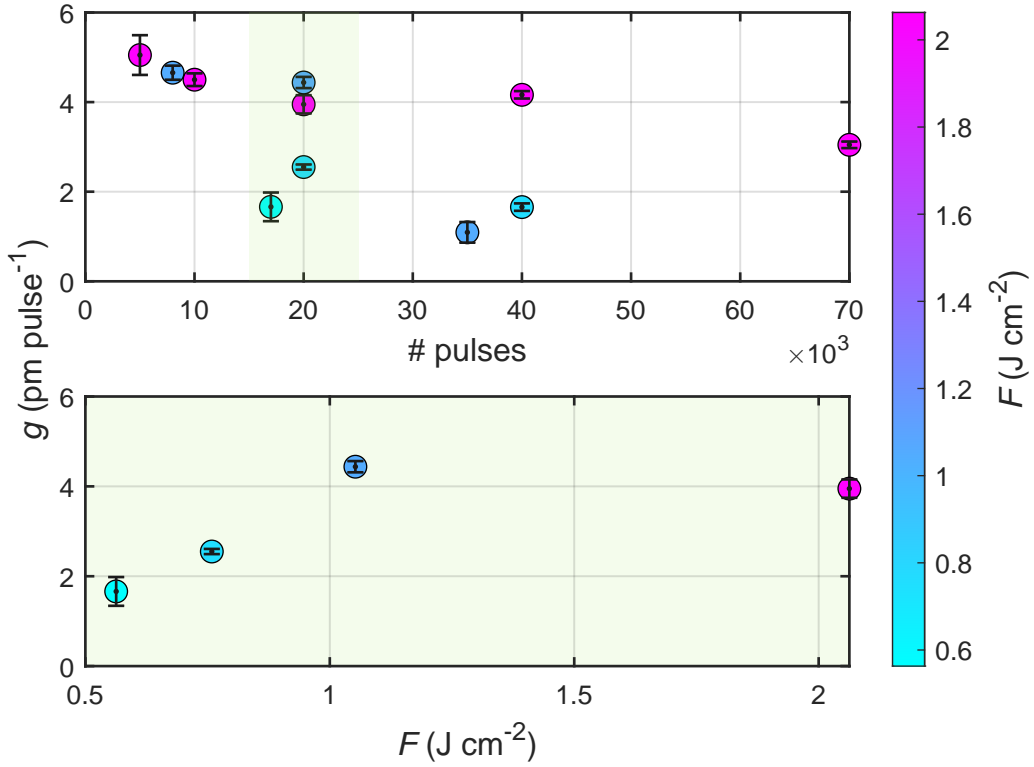


Figure 3.20: Growth rates of the samples from the 1st batch, depending on the pulse number (top) and depending on the laser fluence on the target for an approx. fixed pulse number (bottom). The data points are the mean of the four samples with another orientation each, that were obtained from every process. The errorbar displays the standard deviation.

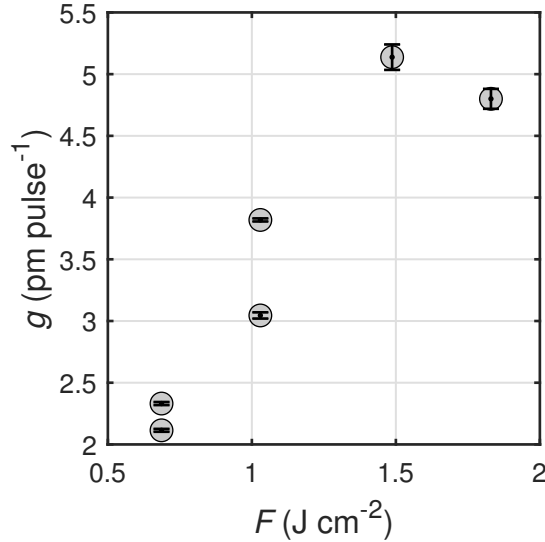


Figure 3.21: Growth rates of samples from the 2nd batch, depending on laser fluence on the target surface. The data points are the mean of thicknesses of the four orientations, similar to Fig. 3.20.

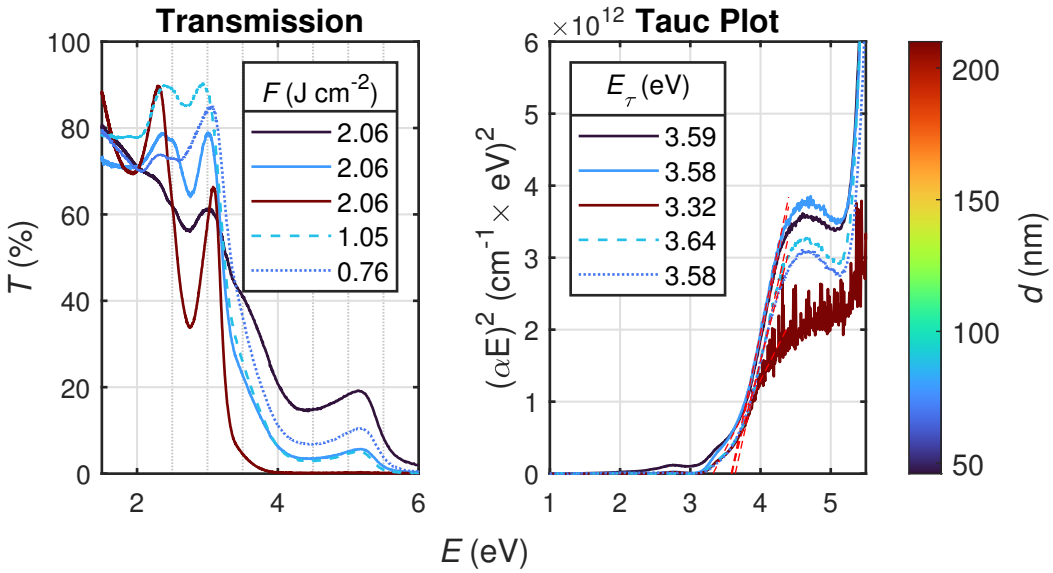


Figure 3.22: Transmission spectra (left) of selected m -plane oriented samples from the 1st batch. The samples differed in thickness and laser fluence on the target surface, achieved by varying lens positions. The TAUC-plot (right) of the mentioned samples, determined by assuming a direct band gap of Cr_2O_3 (cf. 3.1).

In Fig. 3.22, the transmission spectra of selected m -plane oriented samples from the 1st batch are depicted. The fluence does not seem to have a significant influence, however, the thickness is decisive for the shape of the absorption edge. The onset of absorption E_τ is approx. 3.6 eV for all samples of different thickness and fluence. This is in accordance with the value obtained for the samples of the initial Cr_2O_3 batch (cf. 3.1 and Fig. 3.5b). But note that E_τ depends strongly on where the regime for linear fitting is set, so those values are only a rough estimate and should not be confused with the band gap.

Strain for c -plane Thin Films

Appendices

Appendix A

Calculations

A.1 *m*-plane lattice constants

The reflection $(30.\pm 6)$ is a superposition of out-of-plane (30.0) and in-plane $(00.\pm 6)$. The lattice plane distances are

$$q_{\perp}^{(30.\pm 6)} = d_{(30.0)}^{-1} = \sqrt{\frac{4}{3} \frac{3^2}{a^2}} = \sqrt{12}/a, \quad (\text{A.1})$$

$$q_{\parallel}^{(30.\pm 6)} = d_{(00.\pm 6)}^{-1} = \sqrt{\frac{(\pm 6)^2}{c^2}} = 6/c. \quad (\text{A.2})$$

In the y -axis azimuth, $(4\bar{2}.0)$ is a superposition of out-of-plane (30.0) and in-plane $(1\bar{2}.0)$. Note that $(1\bar{2}.0)$ has a -plane character. The lattice plane distances are

$$q_{\perp}^{(4\bar{2}.0)} = d_{(30.0)}^{-1} = \sqrt{12}/a, \quad (\text{A.3})$$

$$q_{\parallel}^{(4\bar{2}.0)} = d_{(1\bar{2}.0)}^{-1} = \sqrt{\frac{4}{3} \frac{1^2 + 2^2 - 2}{a^2}} = 2/a. \quad (\text{A.4})$$

Also in this azimuth, (22.0) is a superposition of out-of-plane (30.0) and in-plane $(\bar{1}2.0)$. The lattice plane distances are

$$q_{\perp}^{(22.0)} = d_{(30.0)}^{-1} = \sqrt{12}/a, \quad (\text{A.5})$$

$$q_{\parallel}^{(22.0)} = d_{(\bar{1}2.0)}^{-1} = \sqrt{\frac{4}{3} \frac{1^2 + 2^2 - 2}{a^2}} = 2/a. \quad (\text{A.6})$$

A.2 *a*-plane lattice constants

The reflection $(22.\pm 6)$ is a superposition of out-of-plane (22.0) and in-plane $(00.\pm 6)$. The lattice plane distances are

$$q_{\perp}^{(22.\pm 6)} = d_{(22.0)}^{-1} = \sqrt{\frac{4}{3} \frac{2^2 + 2^2 - 4}{a^2}} = 2/a, \quad (\text{A.7})$$

$$q_{\parallel}^{(22.\pm 6)} = d_{(00.\pm 6)}^{-1} = 6/c. \quad (\text{A.8})$$

In the y -axis azimuth, (30.0) cannot be represented as a superposition of in-plane and out-of-plane scattering vectors. This is due to the symmetry of the hexagonal lattice. But it is possible to represent it as a superposition of out-of-plane (11.0) and in-plane ($1\bar{1}.0$), multiplied with a factor of 1.5 each. This leads to the calculation of lattice planes via

$$q_{\perp}^{(30.0)} = \frac{3}{2} \cdot d_{1\bar{1}.0}^{-1} = \frac{3}{2} \sqrt{\frac{4}{3} \frac{1^2 + 1^2 - 1}{a^2}} = \frac{3}{2} \cdot \frac{2}{\sqrt{3}}/a = \sqrt{3}/a, \quad (\text{A.9})$$

$$q_{\parallel}^{(30.0)} = \frac{3}{2} \cdot d_{11.0}^{-1} = \frac{3}{2} \sqrt{\frac{4}{3} \frac{1^2 + 1^2 + 1}{a^2}} = \frac{3}{2} \cdot 2/a = 3/a. \quad (\text{A.10})$$

The same holds for the (03.0) reflection: it is a superposition of ($\bar{1}1.0$) and (11.0), multiplied by a factor of 1.5 and one obtains:

$$q_{\perp}^{(03.0)} = \frac{3}{2} \cdot d_{\bar{1}1.0}^{-1} = \sqrt{3}/a, \quad (\text{A.11})$$

$$q_{\parallel}^{(03.0)} = \frac{3}{2} \cdot d_{11.0}^{-1} = 3/a. \quad (\text{A.12})$$

Appendix B

Figures

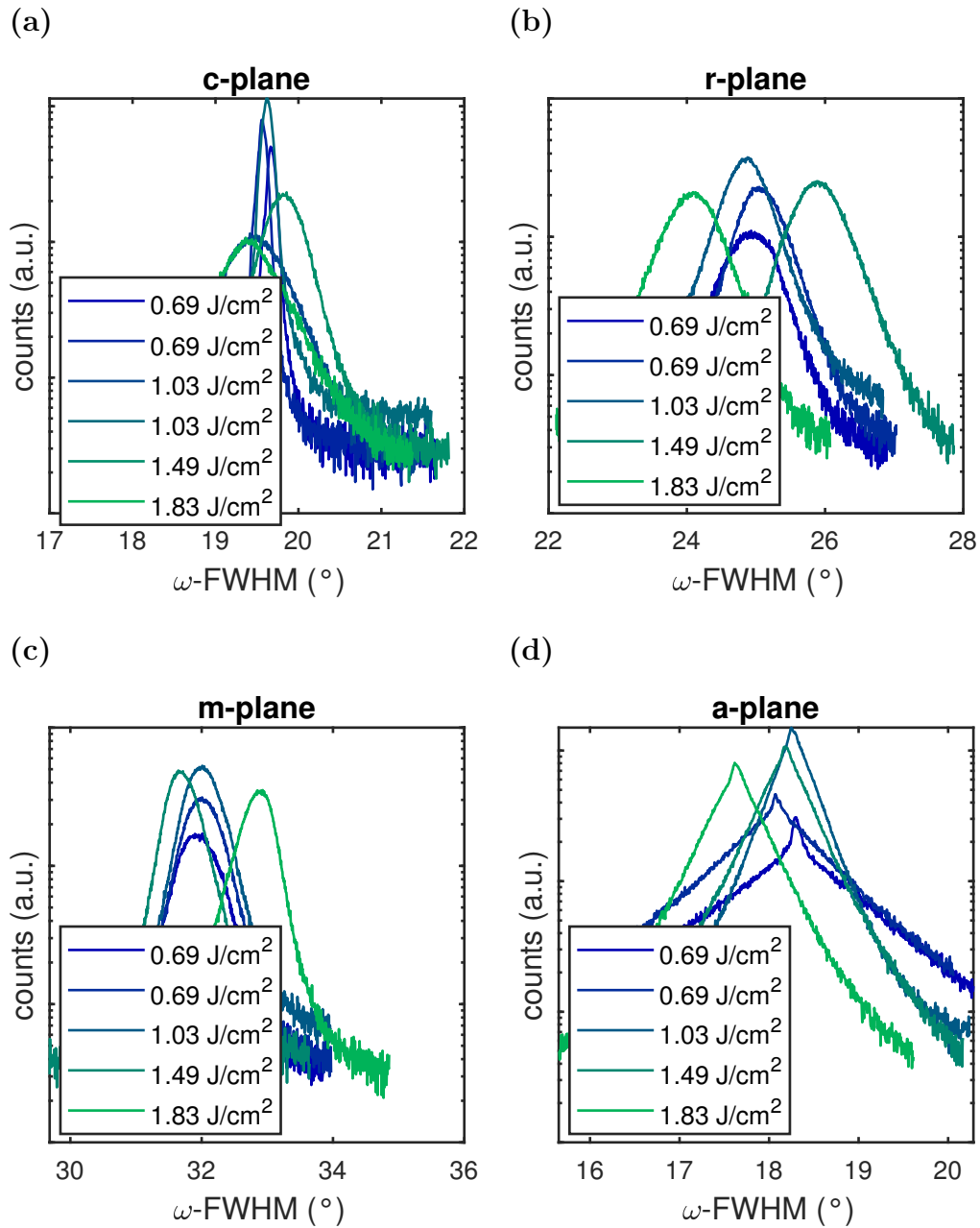


Figure B.1: Diffractogramms from ω -patterns for laser pulse energy.

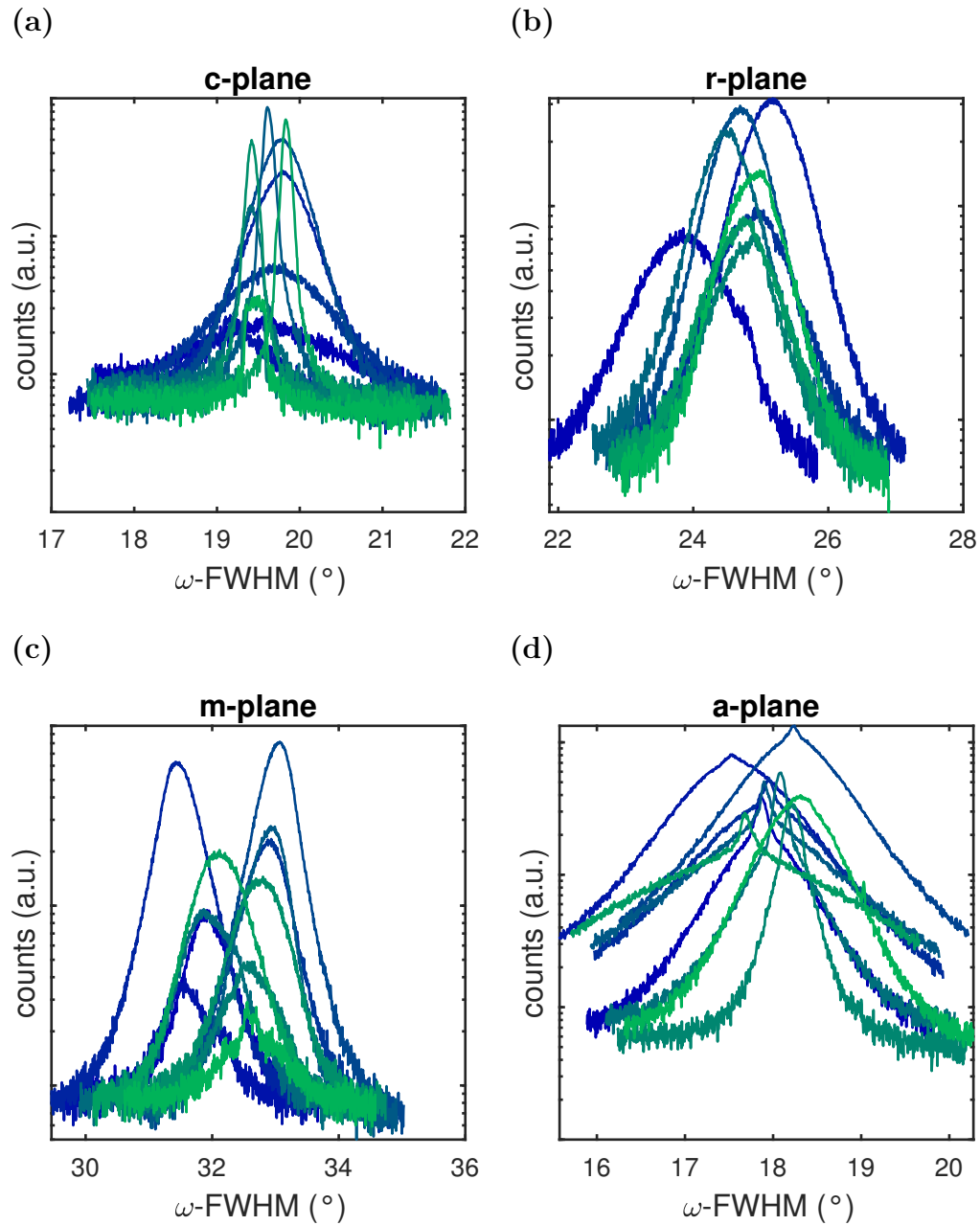


Figure B.2: Diffractogramms from ω -patterns for varying laser focus.

Bibliography

- [1] Neil W. Ashcroft and N. David Mermin. *Solid State Physics*. Saunders College Publishing, 1976. 826 pp.
- [2] George F. Harrington and José Santiso. “Back-to-Basics tutorial: X-ray diffraction of thin films”. In: *Journal of Electroceramics* 47.4 (2021), pp. 141–163. ISSN: 1385-3449, 1573-8663. DOI: [10.1007/s10832-021-00263-6](https://doi.org/10.1007/s10832-021-00263-6).
- [3] Lothar Spieß, ed. *Moderne Röntgenbeugung: Röntgendiffraktometrie für Materialwissenschaftler, Physiker und Chemiker*. 2., überarb. und erw. Aufl. Studium. Wiesbaden: Vieweg + Teubner, 2009. 564 pp. ISBN: 978-3-8351-0166-1.
- [4] Aoife B Kehoe et al. “Assessing the potential of Mg-doped Cr₂O₃ as a novel *p*-type transparent conducting oxide”. In: *Journal of Physics: Condensed Matter* 28.12 (2016), p. 125501. ISSN: 0953-8984, 1361-648X. DOI: [10.1088/0953-8984/28/12/125501](https://doi.org/10.1088/0953-8984/28/12/125501).
- [5] David S. Ginley, ed. *Handbook of Transparent Conductors*. Boston, MA: Springer US, 2011. ISBN: 978-1-4419-1637-2 978-1-4419-1638-9. DOI: [10.1007/978-1-4419-1638-9](https://doi.org/10.1007/978-1-4419-1638-9).
- [6] Anna Hassa, Marius Grundmann, and Holger Von Wenckstern. “Progression of group-III sesquioxides: epitaxy, solubility and desorption”. In: *Journal of Physics D: Applied Physics* 54.22 (2021), p. 223001. ISSN: 0022-3727, 1361-6463. DOI: [10.1088/1361-6463/abd4a4](https://doi.org/10.1088/1361-6463/abd4a4).
- [7] Clemens Petersen et al. “PLD of α -Ga₂O₃ on m-plane Al₂O₃: Growth regime, growth process, and structural properties”. In: *APL Materials* 11.6 (2023), p. 061122. ISSN: 2166-532X. DOI: [10.1063/5.0149797](https://doi.org/10.1063/5.0149797).
- [8] S.I. Stepanov et al. “HVPE growth of corundum-structured α -Ga₂O₃ on sapphire substrates with α -Cr₂O₃ buffer layer”. In: *Materials Physics and Mechanics* 47 (2021), pp. 577–581. DOI: [10.18149/MPM.4742021_4](https://doi.org/10.18149/MPM.4742021_4).
- [9] N. Uekawa and K. Kaneko. “Dopant Reduction in *p*-Type Oxide Films upon Oxygen Absorption”. In: *The Journal of Physical Chemistry* 100.10 (1996), pp. 4193–4198. ISSN: 0022-3654, 1541-5740. DOI: [10.1021/jp952784m](https://doi.org/10.1021/jp952784m).
- [10] P. S. Robbert et al. “Novel electronic and magnetic properties of ultrathin chromium oxide films grown on Pt(111)”. In: *Journal of Vacuum Science & Technology A: Vacuum, Surfaces, and Films* 16.3 (1998), pp. 990–995. ISSN: 0734-2101, 1520-8559. DOI: [10.1116/1.581283](https://doi.org/10.1116/1.581283).
- [11] M.F. Al-Kuhaili and S.M.A. Durrani. “Optical properties of chromium oxide thin films deposited by electron-beam evaporation”. In: *Optical Materials* 29.6 (2007), pp. 709–713. ISSN: 09253467. DOI: [10.1016/j.optmat.2005.11.020](https://doi.org/10.1016/j.optmat.2005.11.020).

- [12] François Lebreau et al. “Structural, Magnetic, Electronic, Defect, and Diffusion Properties of Cr₂O₃: A DFT+U Study”. In: *The Journal of Physical Chemistry C* 118.31 (2014), pp. 18133–18145. ISSN: 1932-7447. DOI: [10.1021/jp5039943](https://doi.org/10.1021/jp5039943).
- [13] Zhishan Mi et al. “The effects of strain and vacancy defects on the electronic structure of Cr₂O₃”. In: *Computational Materials Science* 144 (2018), pp. 64–69. ISSN: 09270256. DOI: [10.1016/j.commatsci.2017.12.012](https://doi.org/10.1016/j.commatsci.2017.12.012).
- [14] Jarnail Singh et al. “Structural, optical and electrical characterization of epitaxial Cr₂O₃ thin film deposited by PLD”. In: *Materials Research Express* 6.10 (2019), p. 106406. ISSN: 2053-1591. DOI: [10.1088/2053-1591/ab3543](https://doi.org/10.1088/2053-1591/ab3543).
- [15] Chun-Shen Cheng, H. Gomi, and H. Sakata. “Electrical and Optical Properties of Cr₂O₃ Films Prepared by Chemical Vapour Deposition”. In: *Physica Status Solidi (a)* 155.2 (1996), pp. 417–425. ISSN: 00318965, 1521396X. DOI: [10.1002/pssa.2211550215](https://doi.org/10.1002/pssa.2211550215).
- [16] Cecilia Guillén and José Herrero. “Structural Changes Induced by Heating in Sputtered NiO and Cr₂O₃ Thin Films as *p*-Type Transparent Conductive Electrodes”. In: *Electronic Materials* 2.2 (2021), pp. 49–59. ISSN: 2673-3978. DOI: [10.3390/electronicmat2020005](https://doi.org/10.3390/electronicmat2020005).
- [17] M. Catti et al. “Electronic, magnetic and crystal structure of Cr₂O₃ by theoretical methods”. In: *Journal of Physics and Chemistry of Solids* 57.11 (1996), pp. 1735–1741. ISSN: 00223697. DOI: [10.1016/0022-3697\(96\)00034-0](https://doi.org/10.1016/0022-3697(96)00034-0).
- [18] Larry W. Finger and Robert M. Hazen. “Crystal structure and isothermal compression of Fe₂O₃, Cr₂O₃, and V₂O₃ to 50 kbars”. In: *Journal of Applied Physics* 51.10 (1980), pp. 5362–5367. ISSN: 0021-8979, 1089-7550. DOI: [10.1063/1.327451](https://doi.org/10.1063/1.327451).
- [19] Elisabetta Arca et al. “Effect of Chemical Precursors On the Optical and Electrical Properties of *p*-Type Transparent Conducting Cr₂O₃:(Mg,N)”. In: *The Journal of Physical Chemistry C* 117.42 (2013), pp. 21901–21907. ISSN: 1932-7447. DOI: [10.1021/jp404230k](https://doi.org/10.1021/jp404230k).
- [20] Valerian Pishchik, Leonid A. Lytvynov, and Elena R. Dobrovinskaya. *Sapphire: Material, Manufacturing, Applications*. Boston, MA: Springer US, 2009. ISBN: 978-0-387-85694-0 978-0-387-85695-7. DOI: [10.1007/978-0-387-85695-7](https://doi.org/10.1007/978-0-387-85695-7).
- [21] M. Marezio and J. P. Remeika. “Bond lengths in the α -Ga₂O₃ structure and the high-pressure phase of Ga_{2-x}Fe_xO₃”. In: *The Journal of Chemical Physics* 46.5 (1967), pp. 1862–1865. ISSN: 0021-9606, 1089-7690. DOI: [10.1063/1.1840945](https://doi.org/10.1063/1.1840945).
- [22] Ruihua Cheng, C.N. Borca, and P.A. Dowben. “Selective Area Chemical Vapor Deposition of Chromium Oxides”. In: *MRS Proceedings* 614 (2000), F10.4.1. ISSN: 0272-9172, 1946-4274. DOI: [10.1557/PROC-614-F10.4.1](https://doi.org/10.1557/PROC-614-F10.4.1).
- [23] Ruihua Cheng et al. “Characterization of the native Cr₂O₃ oxide surface of CrO₂”. In: *Applied Physics Letters* 79.19 (2001), pp. 3122–3124. ISSN: 0003-6951, 1077-3118. DOI: [10.1063/1.1416474](https://doi.org/10.1063/1.1416474).

- [24] Ruihua Cheng et al. “Potential phase control of chromium oxide thin films prepared by laser-initiated organometallic chemical vapor deposition”. In: *Applied Physics Letters* 78.4 (2001), pp. 521–523. ISSN: 0003-6951, 1077-3118. DOI: [10.1063/1.1343846](https://doi.org/10.1063/1.1343846).
- [25] L. Farrell et al. “Conducting mechanism in the epitaxial *p*-type transparent conducting oxide Cr₂O₃:Mg”. In: *Physical Review B* 91.12 (2015), p. 125202. ISSN: 1098-0121, 1550-235X. DOI: [10.1103/PhysRevB.91.125202](https://doi.org/10.1103/PhysRevB.91.125202).
- [26] E. Arca, K. Fleischer, and I. V. Shvets. “Magnesium, nitrogen codoped Cr₂O₃: A *p*-type transparent conducting oxide”. In: *Applied Physics Letters* 99.11 (2011), p. 111910. ISSN: 0003-6951. DOI: [10.1063/1.3638461](https://doi.org/10.1063/1.3638461).
- [27] Alexander Polyakov et al. “Electrical properties of α-Ga₂O₃ films grown by halide vapor phase epitaxy on sapphire with α-Cr₂O₃ buffers”. In: *Journal of Applied Physics* 131.21 (2022), p. 215701. ISSN: 0021-8979, 1089-7550. DOI: [10.1063/5.0090832](https://doi.org/10.1063/5.0090832).
- [28] Alexander Polyakov et al. “Effects of sapphire substrate orientation on Sn-doped α-Ga₂O₃ grown by halide vapor phase epitaxy using α-Cr₂O₃ buffers”. In: *Journal of Physics D: Applied Physics* 55.49 (2022), p. 495102. ISSN: 0022-3727, 1361-6463. DOI: [10.1088/1361-6463/ac962f](https://doi.org/10.1088/1361-6463/ac962f).
- [29] Anna Caricato et al. “Deposition of chromium oxide thin films with large thermoelectromotive force coefficient by reactive pulsed laser ablation”. In: *Journal of Optoelectronics and Advanced Materials* 12 (2010), p. 427.
- [30] Sandhyarani Punugupati, Jagdish Narayan, and Frank Hunte. “Room temperature ferromagnetism in epitaxial Cr₂O₃ thin films grown on r-sapphire”. In: *Journal of Applied Physics* 117.19 (2015), p. 193907. ISSN: 0021-8979, 1089-7550. DOI: [10.1063/1.4921435](https://doi.org/10.1063/1.4921435).
- [31] Elisabetta Arca et al. “Valence band modification of Cr₂O₃ by Ni-doping: creating a high figure of merit *p*-type TCO”. In: *Journal of Materials Chemistry C* 5.47 (2017), pp. 12610–12618. ISSN: 2050-7534. DOI: [10.1039/C7TC03545D](https://doi.org/10.1039/C7TC03545D).
- [32] P. Kofstad and K. P. Lillerud. “On High Temperature Oxidation of Chromium: II . Properties of and the Oxidation Mechanism of Chromium”. In: *Journal of The Electrochemical Society* 127.11 (1980), pp. 2410–2419. ISSN: 0013-4651, 1945-7111. DOI: [10.1149/1.2129481](https://doi.org/10.1149/1.2129481).
- [33] A Holt and P Kofstad. “Electrical conductivity and defect structure of Cr₂O₃. II. Reduced temperatures (<~1000 °C)”. In: *Solid State Ionics* 69.2 (1994), pp. 137–143. ISSN: 01672738. DOI: [10.1016/0167-2738\(94\)90402-2](https://doi.org/10.1016/0167-2738(94)90402-2).
- [34] Robert Schewski et al. “Epitaxial stabilization of pseudomorphic α-Ga₂O₃ on sapphire (0001)”. In: *Applied Physics Express* 8.1 (2015), p. 011101. ISSN: 1882-0778, 1882-0786. DOI: [10.7567/APEX.8.011101](https://doi.org/10.7567/APEX.8.011101).
- [35] Kentaro Kaneko et al. “Progress in α-Ga₂O₃ for practical device applications”. In: *Japanese Journal of Applied Physics* 62 (SF 2023), SF0803. ISSN: 0021-4922, 1347-4065. DOI: [10.35848/1347-4065/acd125](https://doi.org/10.35848/1347-4065/acd125).

- [36] S. J. Pearton et al. “A review of Ga₂O₃ materials, processing, and devices”. In: *Applied Physics Reviews* 5.1 (2018), p. 011301. ISSN: 1931-9401. DOI: [10.1063/1.5006941](https://doi.org/10.1063/1.5006941).
- [37] Duyoung Yang et al. “Epitaxial growth of alpha gallium oxide thin films on sapphire substrates for electronic and optoelectronic devices: progress and perspective”. In: *Electronic Materials Letters* 18.2 (2022), pp. 113–128. ISSN: 1738-8090, 2093-6788. DOI: [10.1007/s13391-021-00333-5](https://doi.org/10.1007/s13391-021-00333-5).
- [38] Kentaro Kaneko et al. “Evaluation of misfit relaxation in α -Ga₂O₃ epitaxial growth on α -Al₂O₃ substrate”. In: *Japanese Journal of Applied Physics* 51 (2R 2012), p. 020201. ISSN: 0021-4922, 1347-4065. DOI: [10.1143/JJAP.51.020201](https://doi.org/10.1143/JJAP.51.020201).
- [39] Rien Jinno et al. “Reduction in edge dislocation density in corundum-structured α -Ga₂O₃ layers on sapphire substrates with quasi-graded α -(Al,Ga)₂O₃ buffer layers”. In: *Applied Physics Express* 9.7 (2016), p. 071101. ISSN: 1882-0778, 1882-0786. DOI: [10.7567/APEX.9.071101](https://doi.org/10.7567/APEX.9.071101).
- [40] Rien Jinno et al. “Crystal orientation dictated epitaxy of ultrawide-bandgap 5.4- to 8.6-eV α -(AlGa)₂O₃ on m-plane sapphire”. In: *Science Advances* 7.2 (2021), eabd5891. ISSN: 2375-2548. DOI: [10.1126/sciadv.abd5891](https://doi.org/10.1126/sciadv.abd5891).
- [41] Anna Hassa et al. “Control of phase formation of (Al_xGa_{1-x})₂O₃ thin films on c-plane Al₂O₃”. In: *Journal of Physics D: Applied Physics* 53.48 (2020), p. 485105. ISSN: 0022-3727, 1361-6463. DOI: [10.1088/1361-6463/abaf7d](https://doi.org/10.1088/1361-6463/abaf7d).
- [42] L. D. Landau and E. M. Lifshitz. *Theory of Elasticity*. Course of Theoretical Physics vol. 7. Pergamon Press Ltd., 1970. 165 pp. ISBN: 978-0-08-057069-3.
- [43] Marius Grundmann. “Elastic theory of pseudomorphic monoclinic and rhombohedral heterostructures”. In: *Journal of Applied Physics* 124.18 (2018), p. 185302. ISSN: 0021-8979, 1089-7550. DOI: [10.1063/1.5045845](https://doi.org/10.1063/1.5045845).
- [44] H.L. Alberts and J.C.A. Boeyens. “The elastic constants and distance dependence of the magnetic interactions of Cr₂O₃”. In: *Journal of Magnetism and Magnetic Materials* 2.4 (1976), pp. 327–333. ISSN: 03048853. DOI: [10.1016/0304-8853\(76\)90044-5](https://doi.org/10.1016/0304-8853(76)90044-5).
- [45] Marius Grundmann. “A most general and facile recipe for the calculation of heteroepitaxial strain”. In: *physica status solidi (b)* 257.12 (2020), p. 2000323. ISSN: 0370-1972, 1521-3951. DOI: [10.1002/pssb.202000323](https://doi.org/10.1002/pssb.202000323).
- [46] Max Kneiß et al. “Strain states and relaxation for α -(Al_xGa_{1-x})₂O₃ thin films on prismatic planes of α -Al₂O₃ in the full composition range: Fundamental difference of a- and m-epitaxial planes in the manifestation of shear strain and lattice tilt”. In: *Journal of Materials Research* 36.23 (2021), pp. 4816–4831. ISSN: 0884-2914, 2044-5326. DOI: [10.1557/s43578-021-00375-3](https://doi.org/10.1557/s43578-021-00375-3).
- [47] Marius Grundmann. *The Physics of Semiconductors: An Introduction Including Nanophysics and Applications*. Graduate Texts in Physics. Cham: Springer International Publishing, 2016. ISBN: 978-3-319-23879-1 978-3-319-23880-7. URL: <http://link.springer.com/10.1007/978-3-319-23880-7>.
- [48] Derek Hull and D. J. Bacon. *Introduction to Dislocations*. 5th ed. Elsevier Ltd., 2011. 268 pp. ISBN: 978-0-08-096673-1.

- [49] M. Grundmann and M. Lorenz. “Anisotropic strain relaxation through prismatic and basal slip in α -(Al, Ga)₂O₃ on R-plane Al₂O₃”. In: *APL Materials* 8.2 (2020), p. 021108. ISSN: 2166-532X. DOI: [10.1063/1.5144744](https://doi.org/10.1063/1.5144744).
- [50] M. Grundmann, T. Stralka, and M. Lorenz. “Epitaxial growth and strain relaxation of corundum-phase (Al,Ga)₂O₃ thin films from pulsed laser deposition at 1000 °C on r-plane Al₂O₃”. In: *Applied Physics Letters* 117.24 (2020), p. 242102. ISSN: 0003-6951, 1077-3118. DOI: [10.1063/5.0030675](https://doi.org/10.1063/5.0030675).
- [51] Michael Lorenz. “Pulsed laser deposition”. In: *Encyclopedia of Applied Physics*. Wiley, 2019. URL: <http://dx.doi.org/10.1002/3527600434.eap810>.
- [52] Holger von Wenckstern et al. “A review of the segmented-target approach to combinatorial material synthesis by pulsed-laser deposition”. In: *Phy. Status Solidi B* 257.7 (2020), p. 1900626. ISSN: 0370-1972, 1521-3951. DOI: [10.1002/pssb.201900626](https://doi.org/10.1002/pssb.201900626).
- [53] V. Srikant, J. S. Speck, and D. R. Clarke. “Mosaic structure in epitaxial thin films having large lattice mismatch”. In: *Journal of Applied Physics* 82.9 (1997), pp. 4286–4295. ISSN: 0021-8979, 1089-7550. DOI: [10.1063/1.366235](https://doi.org/10.1063/1.366235).
- [54] Sofie Vogt et al. “Realization of Conductive n-Type Doped α -Ga₂O₃ on *m*-Plane Sapphire Grown by a Two-Step Pulsed Laser Deposition Process”. In: *physica status solidi (a)* 220.3 (2023), p. 2200721. ISSN: 1862-6300, 1862-6319. DOI: [10.1002/pssa.202200721](https://doi.org/10.1002/pssa.202200721).
- [55] L. J. van der Pauw. “A method of measuring specific resistivity and Hall effect of discs of arbitrary shape”. In: *Philips Research Reports* 13.1 (1958), pp. 1–9.
- [56] Hiroyuki Fujiwara. *Spectroscopic Ellipsometry. Principles and Applications*. Tōkyō: John Wiley & Sons, Ltd, 2007. ISBN: 978-4-621-07253-0.